



LAWRENCE
LIVERMORE
NATIONAL
LABORATORY

The Use of Fractional Accumulated Precipitation for the Evaluation of the Annual Cycle of Monsoons

K. R. Sperber, H. Annamalai

October 1, 2013

Climate Dynamics

Disclaimer

This document was prepared as an account of work sponsored by an agency of the United States government. Neither the United States government nor Lawrence Livermore National Security, LLC, nor any of their employees makes any warranty, expressed or implied, or assumes any legal liability or responsibility for the accuracy, completeness, or usefulness of any information, apparatus, product, or process disclosed, or represents that its use would not infringe privately owned rights. Reference herein to any specific commercial product, process, or service by trade name, trademark, manufacturer, or otherwise does not necessarily constitute or imply its endorsement, recommendation, or favoring by the United States government or Lawrence Livermore National Security, LLC. The views and opinions of authors expressed herein do not necessarily state or reflect those of the United States government or Lawrence Livermore National Security, LLC, and shall not be used for advertising or product endorsement purposes.

The Use of Fractional Accumulated Precipitation for the Evaluation of the Annual Cycle of Monsoons

Kenneth R. Sperber^{1,*} and H. Annamalai²

¹Lawrence Livermore National Laboratory
Program for Climate Model Diagnosis and Intercomparison
P. O. Box 808, L-103
Livermore, CA 94551 USA

²University of Hawai'i
International Pacific Research Center
Honolulu, HI

February 2014

Climate Dynamics

(accepted)

*Corresponding Author

Kenneth R. Sperber
Lawrence Livermore National Laboratory
Program for Climate Model Diagnosis and Intercomparison
P. O. Box 808, L-103
Livermore, CA 94551 USA

Email: sperber1@llnl.gov
Ph: (925) 422-7720
Fax: (925) 422-7675

Abstract Using pentad rainfall data we demonstrate the benefits of using accumulated rainfall and fractional accumulated rainfall for the evaluation of the annual cycle of rainfall over various monsoon domains. Our approach circumvents issues related to using threshold-based analysis techniques for investigating the life-cycle of monsoon rainfall. In the CMIP5 models we find systematic errors in the phase of the annual cycle of rainfall. The models are delayed in the onset of summer rainfall over India, the Gulf of Guinea, and the South American Monsoon, with early onset prevalent for the Sahel and the North American Monsoon. This, in combination with the rapid fractional accumulation rate, impacts the ability of the models to simulate the fractional accumulation observed during summer. The rapid fractional accumulation rate and the time at which the accumulation begins are metrics that indicate how well the models concentrate the monsoon rainfall over the peak rainfall season, and the extent to which there is a phase error in the annual cycle. The lack of consistency in the phase error across all domains suggests that a “global” approach to the study of monsoons may not be sufficient to rectify the regional differences. Rather, regional process studies are necessary for diagnosing the underlying causes of the regionally-specific systematic model biases over the different monsoon domains. Despite the afore-mentioned biases, most models simulate well the interannual variability in the date of monsoon onset, the exceptions being models with the most pronounced dry biases. Two methods for estimating monsoon duration are presented, one of which includes nonlinear aspects of the fractional accumulation. The summer fractional accumulation of rainfall provides an objective way to estimate the extent of the monsoon domain, even in models with substantial dry biases for which monsoon is not defined using threshold-based techniques.

Keywords Summer monsoon rainfall · Annual cycle · Climate model intercomparison · Systematic error · Metrics

1 Introduction

The annual cycle of solar heating is integral to the development of summer monsoons, with the most notable example being that over Asia. Due to its lower heat capacity, the land heats up faster than the ocean giving rise to a land-sea thermal contrast (Li and Yanai 1996). The warm anomalies are accentuated in the upper troposphere, largely due to the presence of the Tibetan Plateau. The ensuing heat low over the continent establishes a pressure gradient that promotes development of the summer monsoon circulation, which carries moisture laden air from the tropical Indian Ocean to the continent. Additionally, the northward displacement of the maximum solar heating promotes off-equatorial convection. The specification of annual cycle forcing by solar radiation suggests that climate models should represent monsoons in a reasonably robust manner. However the system is inherently more complex than the basic interactions outlined above (see the review of Webster et al. 1998). Hence, the interactions among the land surface, ocean, convection, and cloud parameterizations give rise to large scatter in the ability of models to simulate precipitation, including, for example, the climatological seasonal means and the climatological annual cycle of the Asian summer monsoon (Sperber et al. 2013).

One of the key findings of Sperber et al. (2013) was that the onset of the monsoon over India was later than observed in the CMIP3 and CMIP5 20th Century/historical simulations. This analysis was based on a threshold-based technique, and there were numerous examples of models for which the monsoon onset could not be defined because of dry biases in the models. Annual cycle amplitude and phase issues in CMIP5 models have been reported for other monsoon domains. Vizzy et al. (2013) reported substantial biases in the simulation of onset and demise of Sahel rainfall, including cases where the bias was so demonstrable that onset and demise times could not be determined. Over Australia, Coleman et al. (2011) found that the CMIP3 multi-model mean rainfall did not increase as sharply as observed, nor did it decay as rapidly as observed, leading the authors to conclude that on average “precipitation is insufficiently concentrated into the wettest months, with too large a fraction of the annual total falling early and late in the wet season.” They also noted the wide dispersion of the individual models whose peak summer rainfall values ranged from ~25% to 160% of the observed mean. For the North American monsoon the CCSM models analyzed by Cook et al. (2012)

overestimated rainfall throughout the year, while the simulation of the annual cycle for the South American monsoon domain was in better agreement with observations. Bambardi and Carvalho (2009) evaluated the South American monsoon in 10 CMIP3 models. They found that most of the models poorly simulated the annual cycle of precipitation over the Amazon and northwest South America, with the models performing better over central and eastern Brazil.

There are numerous reasons why the annual cycle and the estimated onset time of monsoon rainfall could be misrepresented when threshold-based techniques are employed. For example, a modest dry bias could give rise to an apparent delay in monsoon onset since the overall amplitude of the annual cycle is underestimated. Another possibility for delayed onset is that a model with a realistic annual cycle amplitude might have a phase delay in the annual cycle. Conversely, early onset might arise due to an overestimation of the amplitude of the annual cycle and/or an advance in the phase of the annual cycle. Other impacts of an overestimated (underestimated) annual cycle amplitude of rainfall include overestimation (underestimation) of the duration of the monsoon season when using a threshold-based technique.

It is not our intent to criticize threshold-based techniques for estimating the timing of monsoon onset, peak, withdrawal, and duration. In fact, we believe this approach to be the gold standard for benchmarking the evolution of monsoon rainfall, as it is a very stringent test of a model. As alluded to above, successful simulation of the evolution of monsoon rainfall requires a well simulated annual cycle amplitude and phase. While the annual cycle and its harmonics can be readily analyzed using Fourier approaches (e.g., Kirkyla and Hameed 1989, Gleckler et al. 2006), we present an approach that puts the models “on more equal footing.” Namely, we utilize accumulated rainfall to show model bias, and we use fractional accumulated rainfall to analyze the evolution of monsoon rainfall irrespective of the biases in the amplitude of the annual cycle. Our approach also provides an opportunity for data exploration in terms of how well the models represent the contribution of summer monsoon rainfall to the total annual accumulation, estimating the onset time and its interannual variability, monsoon duration, and for defining the spatial extent of monsoon rainfall.

The models and observations are described in Section 2. In Section 3 we describe the methodology and analyze area-averaged time series for the Asian-Australian, African, and the American monsoon systems. In Section 4 spatial patterns of annual cycle diagnostics are presented, with the summary and discussion presented in Section 5.

2 The Observations and Models

Pentads from the Global Precipitation Climatology Project precipitation (GPCP; Xie et al. 2003) and the Climate Prediction Center Merged Analysis of Precipitation (CMAP; Xie and Arkin 1997a) for 1979-2004 are used to validate the Coupled Model Intercomparison Project-5 (CMIP5) model output. GPCP precipitation is based on microwave, infrared, and rain gauge observations (Huffman et al. 1997), while CMAP is derived from infrared, outgoing longwave radiation, microwave (MSU and SSM/I) and precipitation from NCEP-NCAR reanalysis (Xie and Arkin 1997b). Xie et al. (2003) discuss the construction of the GPCP pentad precipitation, including the differences relative to CMAP that arise due to the adjustments required to ensure consistency between the pentad and monthly precipitation products and the impacts of the different input data sources and merging algorithms. They also note that over the ocean the GPCP pentad data has a dry bias of ~20% compared to atoll gauge data. As seen in Sections 3 and 4, the resulting differences between the GPCP and CMAP data sets impacts their respective annual cycle characteristics. The models are interpreted relative to this observational “uncertainty.”

Table 1 contains basic information on the CMIP5 models (Taylor et al. 2012) used in this study, including horizontal and vertical resolution of the atmospheric and oceanic components. The CMIP5 models were finalized circa 2011. Single realizations for each of the models have been evaluated using the historical simulations. Coleman et al. (2011) found that the climatological annual cycle of monthly rainfall among individual realizations of the same model were robust. This suggests that use of a single realization is justified in the present analysis. Though the simulation period is ~1850-present, the period 1961-99 is analyzed herein. This is the period used by Sperber et al. (2013) in their analysis of Asian summer monsoon. These simulations include the modeling groups best estimates of natural (e.g. solar irradiance, volcanic aerosols) and anthropogenic (e.g. greenhouse gases, sulfate aerosols, ozone) climate forcing during the simulation period. More detailed documentation of the CMIP5 model configurations can be found at: <http://pcmdi9.llnl.gov/esgf-web-fe/live#>

All of the model data has been regridded using bilinear interpolation to the GPCP/CMAP 2.5 degree horizontal grid, and simulated daily precipitation has been averaged into pentads. The

Hadley Centre models utilize a 360-day calendar that results in 72 pentads/year. Therefore, we have interpolated their model data to 73 pentads/year to ensure a direct comparison with observations and the other models. With the exception of the interannual variability, for which pentads for each year are examined, the climatological pentad rainfall is analyzed.

Since our main focus is summer rainfall, the pentads for the Australian and South American domains have been reordered to run from July 2-June 27. In this way, one can directly compare the Southern Hemisphere temporal evolution of the accumulated and fractional accumulated rainfall with that over the Northern Hemisphere. Boreal summer corresponds to pentads 31-55 (June 2-September 30), while Austral summer corresponds to pentads 31-55 (November 29-March 29) of the reordered pentads. Use of a 25 pentad long summer allows for a direct comparison of summertime fractional accumulations across the different domains. Quoted dates are the midpoints of the respective pentads (e.g., January 3 corresponds to the average of data from January 1-5).

We begin with an analysis of area-averaged rainfall, and then present spatial plots for observations and select models. All-India rainfall (AIR) is calculated for the region 65°E-85°E, 7°N-25°N (land only). North Australian (AUS) area-averaged rainfall has been calculated over 120°E-150°E, 20°S-10°S (land only), which is the domain used by Coleman et al. (2011) in their analysis of CMIP3 models. The Sahel region is defined as 10°W-10°E, 13°N-18°N, as in Hourdin et al. (2011), who presented results from the AMMA-Model Intercomparison Project. The longitudinal extent of the Sahel was broader in previous analyses (e.g., Nicholson 1980, Sperber and Palmer 1996), but Rowell et al. (1992) showed that the annual cycle phase is consistent between the west and east Sahel. Though not considered a monsoon domain, the behavior over the Gulf of Guinea (GoG, 10°W-10°E, 0°N-5°N) is considered since the onset of Sahel summer rainfall occurs as a sudden northward transition of convection from the Guinean coast (Hourdin et al. 2010, Cook et al. 2012, Vizy et al. 2013). For the North American monsoon (NAM) we use area-averaged rainfall over the region 112°W-103°W, 20°N-37°N. Over this domain Vera et al. (2006) showed a smooth northward propagation of monsoon onset from early June through mid-July. The South American monsoon (SAM) domain is taken to be 65°W-40°W, 20°S-2.5°S (land only). This region is consistent with the leading spatial patterns of rainfall obtained using univariate and multivariate EOF analyses (Carvalho et al. 2012, Jones and Carvalho 2013, respectively), and for which the annual cycle of rainfall exhibits consistent phase (Grimm 2003).

3 Regionally Averaged Rainfall Time Series

The goal of the section is to present alternative methods for evaluating the annual cycle of rainfall. In Section 3.1 the methodology will be elucidated using AIR, and in Section 3.2 the methodology will be applied to the other domains.

3.1 All-India Rainfall: Illustration of the Fractional Accumulation Methodology

There is large scatter in the ability of models to simulate precipitation, including the climatological seasonal means and climatological annual cycle (Sperber et al. 2013). For example, Fig. 1a shows the climatological annual cycle of pentad AIR. The GPCP and CMAP observations show close agreement in the annual cycle of rainfall. A rapid increase in rainfall occurs at about May 28 (Pentad 30), peaking near 9mm/day from mid-July through mid-August (Pentads 39-46). The CMIP5 models have diverse ability to simulate the observed annual cycle of AIR. The majority of models appear to be late in their simulation of the rapid increase in rainfall, with many models also failing to simulate the observed peak rainfall amounts.

The impact of model dry bias is especially problematic when applying threshold-based techniques for analyzing the ability of the models to simulate the time of monsoon onset, peak, and decay. For example, Sperber et al. (2013) used the approach of Wang and LinHo (2002), in which onset and decay were determined based on a 5mm/day threshold of the relative rainfall rate. Many of the CMIP3 and CMIP5 models analyzed by Sperber et al. (2013) had dry biases, such that this monsoon onset threshold was not simulated. Thus, in these terms, monsoon was not even defined over India and other portions of Asia for models with strong dry biases, and no estimate of onset, peak, and decay dates could be made. While threshold-based techniques are stringent (and important) tests for a model, we demonstrate alternative approaches to model analysis that provide for a uniform analysis of the annual cycle of rainfall.

One popular approach is to standardize the rainfall time series by removing the time mean and dividing by the standard deviation, as seen in Fig. 1b. Using this approach, the scatter has been reduced. The delay in rapid rise of rainfall is still evident for most models, and it is now clear that larger than observed positive rainfall excursions persist into the autumn in the CMIP5

models analyzed. Even so, the time series are still noisy, and the fidelity with which the annual cycle is simulated is not clear from this standardization approach.

More clarity to model performance is gained by plotting the rainfall accumulation (Fig. 1c), which, for a given pentad, is the sum of rainfall up to, and including that pentad. This plot more clearly shows the temporal characteristics of the rainfall and the model bias, which are not as evident in the previous plots. For AIR, there is a factor of 5.2 difference in the annual rainfall accumulation in the suite of CMIP5 models analyzed. To more clearly intercompare the annual cycle behavior, in Fig. 1d we show the fractional accumulated rainfall, in which the accumulated rainfall at each pentad is divided by the total accumulated rainfall at the end of the year (pentad 73). Thus, in relative terms, we are able to analyze how well the models simulate the annual cycle irrespective of differences in their time mean bias and temporal standard deviation. Liebmann and Marengo (2001) developed an accumulated rainfall approach to evaluate the South American monsoon. However, their approach differs from that herein, as they presented the accumulations as departures from the climatological mean such that differences in the amplitudes of the annual cycle were retained.

Some examples of insights gained through the use of the accumulation and fractional accumulation can be seen in Figs. 1e and 1f, where select models and observations are shown. Figure 1e shows that GPCP and CMAP have slight differences in the total accumulation, which when viewed in terms of the fractional accumulation (Fig. 1f) the two observed time series are virtually identical. Importantly, despite the large positive rainfall biases in both of the MIROC-ESM models, when viewed in terms of the fractional accumulation, they closely follow the observed annual cycle from pentad 31 onwards. Furthermore, compared to the MIROC-ESM, the inclusion of chemistry in MIROC-ESM-CHEM has not appreciably affected the annual cycle of AIR. All other models have more substantial biases in the representation of the fractional accumulation. The IPSL-CM5A models show a delay in the annual cycle phase with the rapid fractional accumulation¹ occurring later than observed. The differing horizontal resolutions have not impacted the phasing of the annual cycle accumulation, though the medium resolution model has a larger rainfall accumulation compared to the low resolution model. Similarly, the HadCM3

¹The rapid fractional accumulation refers to the linear growth regime that occurs for fractional accumulations of 0.2-0.8 (0.2-0.6 for the Gulf of Guinea). The linear slope of the rapid fractional accumulation and the time at which the rapid fractional accumulation begins are skill metrics for validating the rainfall accumulation rate and the annual cycle phase during the monsoon. See Section 3.2 for more details.

model has a delayed annual cycle, but it has a more rapid fractional accumulation, exceeding the observed fractional accumulation by pentad 45 (August 11). CSIRO-Mk3.6.0 has the second largest AIR dry bias of the models analyzed. Even so, it has an excess fractional accumulation in the pre-monsoon season (prior to June 2, pentad 31), and the accumulation during summer is not as rapid as observed. Quantification of the rapid fractional accumulation will be reported below.

3.2 Other Monsoon Domains

The observed accumulations and the fractional accumulations for several other monsoon domains and the GoG are shown in Figs. 2a and 2b. Figure 2a indicates that the largest observed accumulation occurs for SAM while the lowest accumulations occur for Sahel and NAM. Unlike the monsoon domains, the GoG rainfall exhibits a semi-annual cycle. The decrease in the rate of the GoG accumulation at about pentad 35 precedes the onset of the monsoon over the Sahel (Hourdin et al. 2010, Cook et al. 2012, Vizzy et al. 2013).

The fractional accumulation reveals interesting details of the evolution of rainfall over these domains (Fig. 2b). Relative to AIR, AUS is similarly phased until about pentad 43, after which it experiences larger fractional accumulations during mid-to-late summer. The rapid fractional accumulation of Sahel rainfall is delayed compared the AIR, but it too experiences larger fractional accumulations during mid-to-late summer. This indicates that equivalent fractional accumulations occur over a shorter period of time for the Australian and Sahel rainfall compared to AIR. Relative to AIR, NAM, SAM, and GoG have larger fractional accumulations prior to summer, and weaker fractional accumulations thereafter. This indicates that rainfall accumulations are comparatively more uniform during the course of the annual cycle for these latter regions.

As indicated above, the rapid fractional accumulation rate gives an indication of how concentrated the rainfall is during the monsoon season. Examination of Fig. 2b indicates that the slope of the rapid fractional accumulation is nearly linear for fractional accumulations between 0.2-0.8 (0.2-0.6 for the Gulf of Guinea). Over this range of fractional accumulations, in Fig. 2c the linear regression slopes are plotted vs. the pentad at which the fractional accumulation first becomes ≥ 0.2 (hereafter p0.2). The p0.2 can be considered as the time of monsoon onset given that the rapid fractional accumulation begins at approximately this time. There is close

agreement between GPCP and CMAP in the magnitude of the slopes, with a one pentad difference in p0.2 for Australian and Gulf of Guinea rainfall (also see Table 2). This diagnostic confirms that the Sahel experiences the most rapid fractional accumulations of the domains considered, with the Gulf of Guinea and South American Monsoon rainfall having the weakest fractional accumulation rates. This diagnostic approach will be applied to the simulations in Fig. 4 to provide skill metrics that indicate how well the models represent the rapid fractional accumulation of rainfall during the monsoon season and phase errors in the annual cycle.

The simulated and observed rainfall accumulations and the fractional rainfall accumulations for AUS, Sahel, GoG, NAM, and SAM are shown in Fig. 3. These plots can be used to interpret a models' ability to simulate the regional monsoons. For all domains the model dispersion far exceeds the differences between GPCP and CMAP. As for AIR (Fig 1c), there is a large dispersion among the models in the simulation of the total rainfall (Figs. 3a-3e). The Sahel has the largest range of simulated annual accumulation, a factor of 10.6, consistent with the dispersion found in the AMMA Model Intercomparison Project (Hourdin et al. 2010). AUS, the GoG, and NAM have ranges with factors of 4.5, 3.3, and 3.2, respectively. SAM has the smallest range, a factor of 2.4, though this domain has the largest area considered, which will smooth out errors in local rainfall amounts.

In terms of the fractional accumulations, there are systematic differences between the observations and the models. For Sahel and NAM (Figs. 3g and 3i), and to a lesser extent AUS (Fig. 3f), the models have excessive pre-monsoon fractional accumulations. Conversely, the GoG and SAM fractional accumulations (Figs. 3h and 3j) are similar to AIR in that the models show a delay in the annual cycle, with the rapid fractional accumulations of summer rainfall occurring later than observed. These biases in the timings and fractional accumulation slopes are clearly represented in Fig. 4 and Table 2. For AIR, GoG, and SAM the majority of models are late by 3+ pentads in simulating the rapid fractional accumulation of rainfall (Figs. 4a, 4d, and 4f). For Sahel² and NAM nearly all models are too early for p0.2 (Figs. 4c and 4e). For AUS, the simulated p0.2 scatters about the observations (Fig. 4b). For AUS, Sahel, NAM and SAM, the earliest (latest) models have the smallest (largest) slopes. For the Sahel, the simulated range of slopes is the largest of the domains considered.

²Early onset is also found for the broader Sahel domain (15°W-37.5°E, 12.5°N-17.5°N) used in the model analysis of Rowell et al. (1992).

The fractional rainfall accumulations of GoG and Sahel reveal another shortcoming of the models (Figs. 3h and 3g). In GoG observations, at about pentad 35 (the vertical line in Fig. 3h) we see that the rapid fractional accumulation of rainfall begins to abate. This abatement is seen as a decreased slope in the fractional accumulation. As the abatement over the GoG occurs, the rapid fractional accumulation of observed Sahel rainfall begins, as seen in Fig. 3g. This heralds the transition of the rainfall from the GoG to the Sahel. The majority of the models exhibit different characteristics. As noted above, over the GoG the models are late in developing the rapid fractional accumulation, and over the Sahel they are early in developing the rapid fractional accumulation. Thus, the models have rapid fractional accumulations over the Sahel, even while rapid fractional accumulations are occurring over the GoG. This result indicates that the models are problematic in simulating the transition of rainfall from the GoG to the Sahel since they misrepresent the phasing of the semi-annual and annual cycle components that characterize the ocean-land interface.

The analysis of regionally-averaged time series indicates that there are systematic biases in representing the pentad at which the rapid fractional accumulation begins ($p_{0.2}$), with the transition between GoG and Sahel being especially poorly represented. The biases are regionally dependent, with Sahel and NAM simulated $p_{0.2}$ earlier than observed, while further south over GoG and SAM the simulated $p_{0.2}$ is later than observed. AIR $p_{0.2}$ is also simulated later than observed. As such, regional process studies will be important for diagnosing the underlying causes of the regionally-specific systematic model biases over the different monsoon domains.

4 Spatial Distributions

The fractional rainfall accumulations provide numerous approaches for assessing the spatial heterogeneity of the annual cycle of rainfall. We can evaluate how well the models simulate the fractional accumulations at specific times in the annual cycle. For instance, in Figs. 1d and 1f we have plotted vertical lines at pentad 31 (June 2) and pentad 55 (September 30), the typical start and end dates for generating boreal summer Asian monsoon climatologies. Figure 1f indicates that at pentad 31 the fractional accumulation is ~ 0.10 , while at pentad 55 the fractional accumulation is ~ 0.85 , indicating that $\sim 75\%$ of the annual mean AIR falls during the boreal summer. Additionally, as demonstrated above, one can assess how well the models represent the

time at which the observations reach a given fractional accumulation (p0.2, Fig. 4). The ability of the models to simulate the spatial distributions of these attributes, including an assessment of the interannual variability will now be presented. Due to the large number of models analyzed, we can only show results from a few models, and in the interest of brevity a more limited set of diagnostics are presented for AUS, Sahel, GoG, NAM and SAM.

4.1 Asian Monsoon

Figures 5a-5d show the fractional accumulation at pentad 31 for GPCP and select models. As of pentad 31, the observations indicate fractional accumulations of about 0.04-0.12 over India, with the lowest values occurring over the northwest of the subcontinent (Fig. 5a). Over Southeast Asia, where the monsoon onset occurs earlier, fractional accumulations up to 0.28 occur. Pentad 31 fractional accumulations of 0.12-0.24 occur over western China and Mongolia, while those >0.32 occur over eastern China and Japan. MIROC-ESM, and to a lesser extent CSIRO-Mk3.6.0, have fractional accumulations over India that are similar to GPCP, including the minima over the northwest of the subcontinent (Figs. 5b and 5d). Conversely, HadCM3, which has a pronounced AIR dry bias (Fig. 1c), underestimates the fractional accumulation over India, where values <0.04 are simulated (Fig. 5c). These models all overestimate the fractional accumulations over western China and Mongolia that extend northeast from India. They do, however, simulate well the fractional accumulation of about 0.40 over eastern China near 25°N - 30°N , and to a lesser extent the tripole pattern over the western Pacific Ocean.

Due to space limitations, we will not show the fractional accumulations at pentad 55 (September 30), the end of the boreal summer. Rather, in Figs. 5e-5h we show the fractional accumulations that occur in boreal summer by subtracting the pentad 31 fractional accumulation from that at pentad 55. As seen in Fig. 5e for GPCP, during boreal summer over 85% of the annual rainfall occurs over northwest India, with values in excess of 70% extending to the northeast over China and Mongolia. The models fail to represent the large fractional accumulation over the latter regions (Figs. 5f-5h). Over India MIROC-ESM gives a good representation of the fractional accumulation (Fig. 5h), while HadCM3 overestimates the fractional accumulation, especially over peninsular India (Fig. 5g). Conversely, CSIRO-Mk3.6.0 underestimates the fractional accumulation over India (Fig. 5f). Over eastern China near 25°N -

30°N less than 50% of the annual rainfall occurs during boreal summer. This is well represented by the models, and corresponds to a location of “nontypical monsoon rainfall” as delineated by Wang and Linho (2002). Figure 5 indicates that the locations that have the lowest fractional accumulations at the start of boreal summer are also the locations where the fractional accumulations during the boreal summer are the greatest.

There is a link between the boreal summer fractional accumulation and the time-mean state. For example, MIROC-ESM has excessive boreal summer fractional accumulations over portions of the Arabian Peninsula and the southern and central Arabian Sea (Fig. 5h). At these locations the model overestimates boreal summer rainfall, which contributes to its low pattern correlation compared to GPCP for the boreal summer rainfall climatology (Sperber et al. 2013, see their Fig. 2c). For CNRM-CM5, these fractional accumulation biases are not present (not shown), and it also simulates the distinct maxima near Burma seen in GPCP (Fig. 5e), consistent with it having the largest pattern correlation with GPCP for the boreal summer rainfall climatology (Sperber et al. 2013, see their Fig. 2b).

The slope of the rapid fractional accumulation and p0.2 give insight into the model performance. As seen in Table 2, CSIRO-Mk3.6.0 has a much weaker slope than GPCP, and this coupled with its time delay in attaining p0.2 is associated with the underestimate of the boreal summer fractional accumulation over India (Fig. 5f). HadCM3 was even later in attaining p0.2, but since it had a much larger slope it overestimated the boreal summer fractional accumulation over India (Fig. 5g). With its excellent representation of the area-averaged fractional accumulation over India (Figs. 1d and 1f), including the slope and p.02, MIROC-ESM well represents the behavior over India. CNRM-CM5 also has an excellent representation of the AIR slope, though p0.2 is delayed by 2 pentads compared to GPCP.

The fractional rainfall accumulation during summer can be used to assess the spatial extent of the monsoon domain. In Figs. 5e-5h the summer fractional accumulations are plotted where they are ≥ 0.50 . Figure 5f indicates that the monsoon domain in CSIRO-Mk3.6.0 includes most of India. This is in the context of this models’ weak annual cycle and strong dry bias (Figs. 1a and 1e), whereas the use of the relative rainfall rate threshold-based technique indicates that monsoon is not present over India in this model, as seen on p. 13 of the Sperber et al. (2013) supplemental material at: http://www-pcmdi.llnl.gov/projects/ken/cmip5_bsisv/fig6_onset.pdf In HadCM3 and MIROC-ESM, Figs. 5g and 5h, the monsoon domain fails to extend into the western Pacific,

where it is present in observations (Fig. 5e; Wang and Ding 2008, Sperber et al. 2013). One perceived negative aspect of this approach is that it does not delineate the northward limit of the Asian summer monsoon domain that absolute rainfall amounts engender. Alternatively, from a beneficial perspective, Fig. 5e demonstrates that further west and north of Korea and into Russia, outside of the traditional monsoon domain, boreal summer rainfall dominates the annual cycle. The models represent the extent of this extratropical feature with some success (Figs. 5f-5h).

We now address the issue of monsoon onset, which is heralded by the large-scale ITCZ migration associated with the annual cycle forcing. As seen in Fig. 1f for AIR, the horizontal line for a fractional accumulation of 0.1 intersects with the vertical line at pentad 31 (June 2), roughly consistent with the observed date of Indian monsoon onset. However, given the spatial heterogeneity of the pentad 31 fractional accumulations over India seen in Fig. 5a, a fractional accumulation of 0.2 more closely corresponds to the mean date of monsoon onset over southern India. Conceptually, as the monsoon sets in, over northwest India there will be an increase from the lower fractional accumulations at pentad 31 to the 0.2 level at later pentads. Therefore, one can consider p0.2 as a proxy for the onset date of the monsoon, as presented in Figs. 6a-6d. For GPCP, onset first occurs over Southeast Asia (Matsumoto 1997), and at later pentads over the South China Sea and over the southern Bay of Bengal (Fig. 6a). A clear progression of onset to the northwest is seen over India, consistent with phasing seen in other observational analyses (Wang and Ding 2008, Sperber et al. 2013). Consistent with the results in Figs. 1d and 1f for India, the CSIRO-Mk3.6.0 and the HadCM3 models attain p0.2 at later pentads than observed (Figs. 6b and 6c), especially over peninsular India and the western Bay of Bengal. The MIROC-ESM gives a more realistic representation of the observed propagation characteristics, especially south of 30°N (Fig. 6d). North of 30°N over China the models are too early to varying degrees.

The monsoon is a robust feature of the annual cycle with the year-to-year variability of the onset time not exhibiting large variation. For example, over Kerala, India the observed onset date has an interannual standard deviation of 8-9 days (Ananthakrishnan and Soman 1988, Joseph et al. 1994). The interannual variability of the onset proxy is shown in Figs. 6e-6h. This is the standard deviation obtained from calculating p0.2 for each year of data. In GPCP, over most of the Asian monsoon land mass the standard deviation is 1-2.5 pentads, whereas over the ocean (the western Arabian Sea, south of 10°N, and the western Pacific) the variability tends to be larger (Fig. 6e). The HadCM3 interannual variability (Fig. 6g) is in good agreement with GPCP,

despite the climatological onset date over India being later than observed (Fig. 6c). MIROC-ESM performs nearly as well, though the variability is slightly underestimated over western India, the eastern Arabian Sea, and the Indian Ocean (Fig. 6h). CSIRO-MK3.6.0 greatly overestimates the variability of monsoon onset over India (Fig. 6f), as do HadGEM2-CC, HadGEM2-ES, and MRI-CGCM3 (not shown). Notably, these latter four models have the largest underestimate of the AIR during the boreal summer (Figs. 1a and 1c). It may be that with the weak Indian monsoon, the onset time there is more variable in models that are not sensitive enough to the annual cycle forcing. The onset variability is due to the phase of the intraseasonal variability and/or the boundary forced signals (ENSO or southern Indian Ocean sea surface temperature) that can affect the timing of the large-scale intertropical convergence zone migration. Models that have a weak response to the annual cycle forcing may be susceptible to boundary forced signals. Additionally, single large rainfall events can give rise to a “bogus onset.” However, determining the mechanism(s) for this bias is beyond the scope of this paper.

4.2 Australia

The peak season rainfall over northern Australia occurs during summer (December-March), as seen in Coleman et al. (2011). Given the reordering of the pentad data to July-June for the Southern Hemisphere, this corresponds to pentads 31-55 (November 29-March 29), analogous to the period of the boreal summer Asian monsoon. Coleman et al. (2011) showed the annual cycle of rainfall averaged over 120°E-150°E, 20°S-10°S for CMIP3 models and observations. The dispersion among the CMIP3 models is similar to that of the CMIP5 models analyzed herein (not shown).

Over northern tropical Australia >75% of the total annual rainfall falls during the monsoon season (Fig. 7a), similar to the boreal summer monsoon over India. CanESM2 and MRI-CGCM3 have similar accumulations, with the former model including the representation of both of the local maxima over northwestern Australia and the Gulf of Carpentaria (Figs. 7b and 7d). CanESM2 has a good representation of the area-averaged fractional accumulation, though with a slight overestimation of the pre-monsoon fractional accumulation (Fig. 3f), despite having a dry bias of ~25-50% in the total annual accumulation depending upon whether the comparison is made with CMAP or GPCP, respectively (Fig. 3a). As seen in Table 2 this model also well

represented the observed rapid fractional accumulation slope and p0.2. MRI-CGM3 has a slightly larger slope than observations which compensates for its deficit in pre-monsoon fractional accumulation and hence late p0.2 (Fig. 7d). While MIROC-ESM performed well over the Asian summer monsoon domain (Figs. 5 and 6), it underestimates the summer accumulation over northern Australia (Fig. 7c), consistent with its weak slope and its early p0.2 (Table 2).

Compared to GPCP (Fig. 7e), the interannual variability of the onset pentad is well represented in CanESM2 and MRI-CGCM3 (Figs. 7f and 7h), with standard deviations of about 1.5-3 pentads over the northern tropics, and much larger variability over the Maritime Continent, and over central/southern Australia where extratropical frontal activity dominates. MIROC-ESM has a local minima in onset variability over northwestern Australia, but the observed enhanced interannual variability to the north and south are not well represented (Fig. 7g). Thus, in MIROC-ESM, the Australian monsoon is not nearly as well represented compared to its simulation of the Asian monsoon. This attests to the need to understand the differing controlling mechanisms of the regional monsoons.

4.3 Sahel and Gulf of Guinea

Of the domains considered, Sahel monsoon rainfall is uniquely problematic. Close inspection of the fractional accumulations in Fig. 3g indicates that numerous models exhibit a semi-annual cycle over this region, more akin to that expected for the Gulf of Guinea region (Fig. 3h). This can also be seen in the regionally averaged rainfall (Fig. 8a), and in the standardized rainfall anomalies (Fig. 8b). Consistent with the fractional accumulation, the majority of models have too much pre-monsoon rainfall, and too little during the monsoon season. MIROC-ESM-CHEM and MIROC-ESM are particularly problematic in this respect. As seen for GPCP in Fig. 8c (and as with the Asian and Australian monsoons) the fractional accumulations at the start of summer (pentad 31) are typically less than 0.12 over the monsoon domain. However, MIROC-ESM-CHEM has fractional accumulations in excess of 0.24 over the Sahel at this time (Fig. 8d), including values in excess of 0.44 near 20°N that far exceed the observed fractional accumulations. Compared to GPCP (Fig. 8e), in which boreal summer fractional accumulations (pentad 55 – pentad 31) reach upwards of 0.9-0.95, the MIROC-ESM-CHEM model only has fractional accumulations of 0.55-0.7. The overestimate in pre-monsoon rainfall and the

underestimate of boreal summer fractional accumulations are consistent with the slope and p0.20 values in Fig. 4c and Table 2. These biases are reduced in the MIROC5 model (not shown), which has a modified convection scheme, among other changes, compared to the MIROC-ESM's.

As mentioned previously, there is a strong semi-annual cycle of rainfall over the Gulf of Guinea (Fig. 3h). The fact that the models incorrectly exhibit a semi-annual component over the Sahel indicates that they are not simulating the strong north-south gradients of variability that dominate the observations.

The interannual variability of onset using yearly p0.2 is shown in Fig. 9. The Sahel is a narrow region, extending from 13°N-18°N. As seen in the observations (Fig. 9a), the onset at the northern periphery of the Sahel has larger interannual variability than the southern periphery. This is also true of the models; for example the IPSL-CM5A-LR model (Fig. 9b). However, in MIROC-ESM-CHEM (Fig. 9c), which has the largest bias in terms of pre-monsoon rainfall and a pronounced semi-annual cycle (Figs. 3g, 8a, and 8b), there is an overestimate of variability over the southern portion of the eastern Sahel (east of 0°E). Over the ocean, south of Guinea coast, the models have lower variability than observed.

4.4 North American Monsoon and South American Monsoons

Of the monsoon regions analyzed, NAM is the second driest, being barely wetter than the Sahel, while SAM is 30% wetter than AIR (Fig. 2a). Both American monsoon domains differ from the other monsoon domains in that they have the weakest fractional accumulation slope (Fig. 2c, Table 2) indicating that their rainfall is comparatively more evenly distributed during the annual cycle. The models also have different systematic errors with respect to the phase of the annual cycle. For NAM the models have excessive fractional accumulations early in the year (Fig. 3i). For SAM the models are late, as indicated by the underestimated fractional accumulations from ~July-November (Fig. 3j).

In addition to the p0.2 data in Table 2, and in Figs. 4e and 4f that confirm the NAM and SAM advanced and delayed annual cycles, there is another data exploration approach that can be used to evaluate the spatial distribution of these temporal biases. This firstly begins with the GPCP fractional accumulation at pentad 31 (or any other pentad at which one is interested in),

for NAM and SAM (Figs. 10a and 10e). For NAM the fractional accumulations at this time are similar to those near India (Fig. 5a), with values typically ≤ 0.16 . For SAM, values in this range are only found at the northeast coast of Brazil, with values ≥ 0.24 over the interior of the continent. We next use the observed pentad 31 fractional accumulation pattern as a reference field to determine the first pentad at which the models fractional accumulations are \geq GPCP fractional accumulations. Given a perfect model, the diagnosed field would have a uniform value of 31. Figures 10b and 10f indicate that there are differences between the GPCP and CMAP data sets, with CMAP attaining the pentad 31 fractional accumulations within about 1 pentad of GPCP over most of the region. The most critical (monsoon-related) discrepancy is over western Mexico near the Gulf of California where CMAP peaks earlier than GPCP. This discrepancy was not evident in Fig. 3i given the large area over which the NAM average annual cycle was calculated. For the area-averaged NAM index, GFDL-ESM2G has a similar fractional accumulation to GPCP and CMAP at pentad 31 (Fig. 3i). However, the GFDL-ESM2G spatial pattern indicates that this was in part due to compensating errors (Fig. 10c), with the model attaining the GPCP pentad 31 fractional accumulation too early over Mexico, and too late over the Pacific Ocean. Our results indicate that this and most of the other models have similar discrepancies in representing the annual cycle of rainfall between land and ocean over this region. INMCM4 is a demonstrable example of the early fractional accumulations for NAM (Fig. 10d). For SAM, HadGEM2-ES performed reasonably well in estimating the timing, though there is an east-west gradient in the simulated phase of the annual cycle (Fig. 10g). Yin et al. (2012) found that the HadGEM2 models had an “adequate” simulation of the pattern of the wet season rainfall climatology and the annual cycle of precipitation over Amazonia. IPSL-CM5A-MR (Fig. 10h) and IPSL-CM5A-LR (not shown) are similar to many of the other models, with SAM annual cycle phasing that is later than GPCP and CMAP. Yin et al. (2012) noted that the IPSL-CM5A-LR model had a poor representation of the annual cycle of precipitation over (a slightly more restricted) SAM.

For NAM and SAM the fractional accumulations during summer (pentad 55 – pentad 31) are shown in Fig. 11. For NAM, and especially SAM (Figs. 11a and 11d), the maximum observed summer fractional accumulations are lower than those near India (Fig. 5e). For SAM the values are more similar to those over East Asia (0.6 – 0.7). For NAM most models tend to underestimate the boreal summer fractional accumulations, given their systematic underestimate

of the rapid fractional accumulation rate (slope) seen in Fig. 4e and Table 2. For example, GFDL-ESM2G slightly underestimates the fractional accumulation (Fig. 11b), while this bias is more severe in INMCM4 (Fig. 11c), consistent with their slopes being ~82% and ~36% of that observed. For SAM, HadGEM2-ES has an Austral summer fractional accumulation and slope consistent with observations (Fig. 11e), whereas IPSL-CM5A-MR (Fig. 11f) is more typical of the remaining models for which the fractional accumulation and slope are larger than observed.

Even given the shortcomings in representing the phase of the annual cycle and the summer fractional accumulation (Figs. 10 and 11), Fig. 12 indicates that the models reasonably represent the interannual variability of p0.2. For NAM the interannual standard deviation is ~1.5-2.5 pentads over the East Pacific near 10°N, Central America, and southern Mexico, with greater variability over northern Mexico and the southwest United States (Figs. 12a – 12c). For SAM, the largest variability occurs closest to the coast, with lower variability over the interior of the continent (Figs. 12d – 12f). The consistency between simulated and observed interannual variability indicates that the annual cycle phase errors are a robust feature of the simulations.

4.5 Monsoon Duration

In the fractional accumulation approach, monsoon duration can be calculated using two methods, with each method providing insight into different aspects of model bias. These approaches directly target the annual cycle by assessing how long it takes to achieve the following benchmark fractional accumulations associated with (1) the rapid fractional accumulation, and (2) the observed fractional accumulations at the start and end of summer (pentads 31 and 55 in observations). These respective meanings of “duration” are inherently different than that obtained from the relative rainfall rate threshold-based technique. In this latter case, which is related to rainfall intensity, regions of climatologically lower rainfall rate achieve the specified threshold less frequently, if at all. Thus, at these locations the monsoon duration is systematically shorter than locations where the climatological rainfall rate is larger.

Method 1 follows from the calculation of the slopes in Table 2 that quantify the rapid fractional accumulations in the range 0.2 to 0.8 (0.2 to 0.6 for GoG). As initially presented in Section 3.2, p0.2 is the time of onset of the rapid fractional accumulation, and likewise p0.8 is the time at which the rapid fractional accumulation abates. Using these times, the duration of the

rapid fractional accumulation can be calculated as $1 + p_{0.8} - p_{0.2}$. The duration is inversely proportional to the slope, with the durations in Figs 13a-13d reflecting the spatial (in)homogeneity of the rapid fractional accumulation rate.

For GPCP (Fig. 13a) and CMAP (not shown), the longest durations tend to occur over the South China Sea, eastern China, and the western Pacific. From Southeast Asia inland to the north and west *over the monsoon domain* the durations become predominantly shorter, especially over northwest India. This gross structure is similar to the pattern of the durations obtained from the Wang and Linho (2002) threshold-based technique (Sperber et al. 2013). Even so, we do not expect a one-to-one correspondence with the threshold-based durations that measure the length of time that a relative rainfall rate $\geq 5\text{mm/day}$ is sustained, with drier areas thus having shorter duration. MIROC-ESM (Fig. 13d) shows close correspondence to GPCP, as does CNRM-CM5 which has a more realistic estimate of the short duration near northwest India and northeast China (not shown). HadCM3 has a decidedly shorter duration over India (Fig. 13c), consistent with its annual cycle in Fig. 1a and its large slope (Table 2). For method 1 the general finding is that where a model underestimates (overestimates) the summer fractional accumulation (Figs. 5e-5h, 7a-7d, 8e-8f, and 11) the duration is longer (shorter) than the nominal 25 pentad duration.

Method 2 evaluates the models directly against the observations. The method 2 duration is the time the model takes to go from the *observed* fractional accumulation at the start of summer (pentad 31) to the *observed* fractional accumulation at the end of summer (pentad 55). Following on from the analysis approach for NAM and SAM presented in Fig. 10, the GPCP pentad 31 and pentad 55 fractional accumulation patterns are used as a reference fields from which we determine the pentads at which the models fractional accumulations reach the *observed* fractional accumulations. Thus, the method 2 duration is calculated as $1 + \text{pentad the model reaches the GPCP pentad 55 fractional accumulation} - \text{pentad the model reaches the GPCP pentad 31 fractional accumulation}$. For a perfect model, the duration would be 25 at all grid points. Unlike method 1, method 2 accounts for nonlinear aspects of the fractional accumulation. For example, this is clearly seen for AIR from CSIRO-Mk3.6.0 in Fig. 1f. At pentad 31 the observed fractional accumulation is ~ 0.1 . CSIRO-Mk3.6.0 attains this fractional accumulation at pentad 21, with very little fractional accumulation until pentad 33. At pentad 55 the observed fractional accumulation is ~ 0.85 . CSIRO-Mk3.6.0 attains this fractional accumulation at pentad 63. Thus, it takes the model 43 pentads to achieve the summer fractional accumulation that occurred in 25

pentads in GPCP. The longer duration in CSIRO-Mk3.6.0 is due to too much pre-monsoon fractional accumulation of rainfall, the subsequent delay until the rapid fractional accumulation begins, and then the underestimate of the slope of the rapid fractional accumulation. Thus the method 2 diagnostic approach provides a synthesis of the model errors in the annual cycle since it gives information on the phase of the monsoon (the times at which the observed fractional accumulations at pentads 31 and 55 are attained) and its duration.

As seen in Fig. 13e, the method 2 CMAP durations are within 1 pentad of GPCP *over the monsoon domain (with the exception of the West Pacific)*. For the models, over large portions of the Eurasian continent the simulated durations are distinct from the observational uncertainty. The typical tendency is for the models to require longer durations than observed north of $\sim 30^{\circ}\text{N}$ (Figs. 13f-13h). Over India the durations can differ markedly from model to model, with CSIRO-Mk3.6.0 having longer durations than observed (Figs. 13f). Conversely, HadCM3 has shorter than observed durations over India (Fig. 13g). This is consistent with the results in Fig. 1f, arising due to (1) a delay in the annual cycle with the model reaching the observed pentad 31 fractional accumulation later than observed, and (2) the larger than observed rapid fractional accumulation rate that causes the model to attain the observed pentad 55 fractional accumulation sooner than observed. For MIROC-ESM the duration is shorter (longer) than observed over southern (northern) India (Fig. 13h) with this error compensation giving rise to its' close agreement to the GPCP fractional accumulation for the area-averaged AIR (Fig. 1f).

Examples of the method 2 durations for the other monsoon domains are presented in Fig. 14. For Australia, north of 20°S over land, CanESM2 and MRI-CGCM3 have similar patterns with longer durations over the western portion of the continent (Figs. 14a-14b). The longer durations here are within the observational uncertainty based on the CMAP method 2 durations (not shown). South of 20°S , outside of the core monsoon domain, the model behaviors differ, with CanESM2 having longer durations than MRI-CGCM3, since the former (latter) model reaches the observed pentad 31 fractional accumulation before (after) GPCP and CMAP. That both models have a good representation of the Austral summer fractional accumulation (the models fractional accumulation between pentads 31-55) over the core monsoon domain (Figs. 7b and 7d) can be understood from their area-averaged fractional accumulations in Fig. 3f. At pentad 31 CanESM2 and observations are about to begin their rapid fractional accumulation, which at about pentad 51 abates with low fractional accumulations thereafter. Conversely, MRI-CGCM3

has a phase delayed annual cycle, with the rapid fractional accumulation not occurring until about pentad 37, and persisting through pentad 55, unlike observations. Thus, in the instance in which the Austral summer is defined as occurring between pentads 31-55, the nonlinear regime in MRI-CGCM3 occurs at the beginning of the season (Fig. 3f), while in observations and CanESM2, it occurs at the end of the season.

For both Sahel and NAM there are substantial differences between GPCP and CMAP in the method 2 durations. CMAP has longer durations over the Sahel (Fig. 14c) and over northwest Mexico (Fig. 14e). Despite the observational differences, MIROC-ESM-CHEM (INMCM4) has substantially longer durations than observed over the Sahel (NAM) as seen in Fig. 14d (Fig. 14f). This is consistent with both models underestimating the boreal summer fractional accumulation (Fig. 8f for MIROC-ESM-CHEM over the Sahel; not shown for INMCM4 over NAM), and the underestimation of the respective rapid fractional accumulation slopes (Table 2).

For SAM, the method 2 durations for HadGEM2-ES and IPSL-CM5A-MR (Figs. 14g-14h) are consistent with the pentads at which the models reach the GPCP fractional accumulations at pentad 31 (Figs. 10g-10h). IPSL-CM5A-MR and IPSL-CM5A-LR (not shown) systematically underestimate the method 2 duration as a consequence of their overestimation of the rapid fractional accumulation slope (Table 2) in conjunction with its delay in the annual cycle phase. For HadGEM2-ES and HadGEM2-CC (not shown) the excellent agreement of the area-averaged SAM fractional accumulation (Fig. 3j) arises due to some error compensation over the SAM spatial domain. Over the southeastern part of the SAM the model has method 2 durations similar to GPCP, while over eastern-most (northern-central) Brazil the model has shorter (longer) durations where it is late (early) in attaining the GPCP pentad 31 fractional accumulation (Fig. 10g).

From the point of model diagnosis, method 2 provides additional insight compared to method 1. Method 1 is a diagnostic that gives much the same information as the rapid fractional accumulation slope, and it bears gross similarity to threshold-based estimates in terms of monsoon duration. Method 2 is an integrator of model error in terms of the whether the annual cycle is advanced or delayed in association with the rate at which the rapid fractional accumulation occurs. That is, method 2 provides insight into the fidelity of the model representation of pre-monsoon and post-monsoon rainfall and the representation of the rate of the

evolution of summer monsoon rainfall, including the non-linear behavior, as illustrated by CSIRO-Mk3.6.0 for AIR, and CanESM2 and MRI-CGCM3 over AUS.

5 Discussion

The primary motivation for this study was to develop an alternative diagnostic strategy for the evaluation of the annual cycle over monsoon regions, where enormous swings in rainfall are observed. Since monsoon evolution is typically evaluated using threshold-based techniques, models with dry biases are especially at a disadvantage since the observed threshold for defining monsoon may never be reached (Sperber et al. 2013). The fractional accumulation approach we propose circumvents the sampling issue that threshold-based techniques impose, and provides for an elucidation of systematic error in the life-cycle of monsoons across all models since the biases in absolute rainfall are removed. Thus, our approach is useful for assessing a models' monsoon behavior, including onset, duration, spatial extent, and errors in annual cycle phase irrespective of a models' bias in the amplitude of the annual cycle.

Despite the use of annual cycle solar forcing in all models, our study reveals that there is diverse skill in simulation of the annual cycle of rainfall over the numerous monsoon domains. Simple area-averaged time series indicate there are numerous outliers in the ability to simulate climatological annual cycle rainfall accumulations for all domains. The fractional accumulations demonstrate that in many cases solving the problem is not just a matter of increasing (decreasing) rainfall over monsoon regions that have dry (wet) biases, but biases in the phase of the annual cycle are also present, and need to be remedied. For example, our approach clearly demonstrates that most models have a delay in the monsoon onset for AIR, GoG, and SAM, and early onset for the Sahel and NAM. The lack of consistency in the bias across all domains suggests that a "global" approach to the study of monsoons may not be sufficient to rectify the regional differences. Rather, regional process studies are necessary for diagnosing the underlying causes of the regionally-specific systematic model biases over the different monsoon domains.

Our approach also quantifies the fractional accumulation rates that highlight systematic differences in life-cycle evolution and timing among the regional monsoons. The spatial patterns indicate the agreement between models and observations in area-average time series can sometimes be the result of compensating regional error. The largest errors in this respect are due

to the models being unable to represent the observed behavior over land vs. ocean, especially for the Sahel and the Gulf of Guinea, and NAM. Even though biases in phase are present, most models exhibit interannual variability of monsoon onset that is consistent with observations over land, typically about 1.5-2.5 standard deviations. The exceptions tend to be the models with the strongest dry biases over land (Figs. 1c and 3a, 3b, and 3e), where the interannual variability is overestimated.

No single model performs well for all domains. Future effort will be devoted to evaluating the possibility of domain interdependencies, especially for the Asian-Australian monsoon system, which can be viewed as a migration of the Intertropical Convergence Zone (ITCZ). For example, MIROC-ESM performs well over India (Figs. 1f and 5d), but its boreal summer monsoon domain does not extend into the South China Sea and the western Pacific (Fig. 5e) as observed. This model also has problems in representing the Australian summer monsoon, (Figs. 7c and 7g), suggesting that there may be large-scale biases that adversely affect the monsoon simulation over the western subtropical Pacific. One possibility is that the poleward migration of the sea surface temperature over this domain may not be well simulated, thus impacting the propagation characteristics of the ITCZ (Annamalai et al. 2014).

Additionally, work is needed to evaluate how large-scale biases impact small-scale processes (e.g., convection) in the models. Other insight may be forthcoming by determining if there is a relationship between the slope of the rapid fractional accumulation and the characteristics of the spatio-temporal variability and intensity of rainfall. For example, do cases of delayed onset and excessive rapid fractional accumulation suggest too frequent and/or overly intense rain events?

In future work we will also use the fractional accumulation approach to analyze the impact of anthropogenic climate change on the life-cycle of the monsoon. The approach will provide for an assessment of whether the fractional accumulation rate may change during the summer monsoon, and a determination of possible changes in the length and phase of the monsoon season relative to the 20th Century/historical runs.

Acknowledgements. We thank the reviewers for bringing to our attention additional relevant literature, and for suggesting enhancements and clarifications that have improved the paper. We thank Charles Jones for input on the selection of the area-averaged SAM domain. K. R. Sperber was supported by the Office of Science (BER), U.S. Department of Energy through Lawrence

Livermore National Laboratory contract DE-AC52-07NA27344. H. Annamalai was supported by the Office of Science (BER) U.S. Department of Energy, Grant DEFG02-07ER6445, and also by three institutional grants (JAMSTEC, NOAA and NASA) of the International Pacific Research Center. We acknowledge the World Climate Research Programme's Working Group on Coupled Modelling, which is responsible for CMIP, and we thank the climate modeling groups (listed in Table 1 of this paper) for producing and making available their model output. For CMIP the U.S. Department of Energy's Program for Climate Model Diagnosis and Intercomparison provides coordinating support and led development of software infrastructure in partnership with the Global Organization for Earth System Science Portals.

References

- Ananthakrishnan R, Soman MK (1988) The onset of the southwest monsoon over Kerala: 1901-1980. *J Climatology* 8:283-296
- Annamalai H, Mehari M, Sperber KR (2014) A recipe for ENSO-monsoon diagnostics in CMIP5 models. *J Clim* (in preparation)
- Bambardi RJ, Carvalho LMV (2009) IPCC global coupled model simulations of the South America monsoon system. *Clim Dyn* 33:893-916. doi:10.1007/s00382-008-0488-1
- Carvalho LMV, Jones C, Posadas AND, Quiroz R, Bookhagen B, Liebmann B (2012) Precipitation characteristics of the South American monsoon system derived from multiple datasets. *J Clim* 25:4600-4620. doi:10.1175/JCLI-D-11-00335.1
- Coleman RA, Moise AF, Hanson LI (2011) Tropical Australian climate and Australian monsoon as simulated by 23 CMIP3 models. *J Geophys Res* 116:D10116. doi:10.1029/2010JD015149
- Cook KH, Meehl GA, Arblaster JM (2012) Monsoon regimes and processes in CCSM4. Part II: African and American monsoon systems. *J Clim* 25:2609-2621. doi:10.1175/JCLI-D-11-00185.1
- Gleckler PJ, Sperber KR, AchutaRao K (2006) Annual cycle of global ocean heat content: observed and simulated. *J Geophys Res* 111:C06008. doi:10.1029/2005JC003223
- Grimm AM (2003) The El Nino impact on the summer monsoon in Brazil: regional processes versus remote influences. *J Clim*, 16:263-280
- Hourdin F, Musat I, Grandpeix J-Y, Polcher J, Guichard F, Favot F, Marquet P, Boone A, Lafore J-P, Redelsperger J-L, Ruti PM, Dell'aquila A, Filiberti M-A, Pham M, Doval TL, Traore AK, Gallee H (2010) AMMA-model intercomparison project. *Bull. Amer. Meteor. Soc* 91:95-104. doi:10.1175/2009BAMS2791.1
- Huffman GJ, Adler RF, Arkin P, Chang A, Ferraro R, Gruber A, Janowiak J, McNab A, Rudolf B, Schneider U J (1997) The global precipitation climatology project (GPCP) combined precipitation dataset. *Bull Amer Meteor Soc* 78:5-20
- Jones C, Carvahlo LMV (2013) Climate change I the South American monsoon system: present climate and CMIP5 projections. *J. Clim* doi:10.1175/JCLI-D-12-00412.1

776 Joseph PV, Eischeid JJ, Pyle RJ (1994) Interannual variability of the onset of the Indian summer
777 monsoon and its association with atmospheric features, El Nino, and sea surface temperature
778 anomalies. *J Clim* 7:81-105

779 Kirkyla KI, Hameed S (1989) Harmonic analysis of the seasonal cycle in precipitation over the
780 United States: a comparison between observations and a general circulation model. *J Clim*
781 2:1463-1475

782 Li CF, Yanai M (1996) The onset and interannual variability of the Asian summer monsoon in
783 relation to land sea thermal contrast. *J Clim* 9:358–375

784 Liebmann B, Marengo JA (2001) Interannual variability of the rainy season and rainfall in the
785 Brazilian Amazon basin. *J Clim* 14:4308-4318

786 Matsumoto J (1997) Seasonal transition of summer rainy season over Indochina and adjacent
787 monsoon regions. *Adv Atmos Sci* 14:231–245

788 Nicholson SE (1980) The nature of rainfall fluctuations in subtropical west Africa. *Mon. Wea.*
789 *Rev.*, 108, 473-487. *J Clim* 7:81-105

790 Rowell DP, Folland CK, Maskall K, Owen JA, Ward MN (1992) Modelling the influence of
791 global sea surface temperatures on the variability and predictability of seasonal Sahel
792 rainfall. *Geophys Res Lett* 19:905-908

793 Sperber KR, Palmer TN (1996) Interannual tropical rainfall variability in general circulation
794 model simulations associated with the atmospheric model intercomparison project. *J Clim*
795 9:2727-2750

796 Sperber KR, Annamalai H, Kang I-S, Kitoh A, Moise A, Turner A Wang, B, Zhou T (2013) The
797 Asian summer monsoon: an intercomparison of CMIP5 vs. CMIP3 simulations of the late
798 20th century. *Clim Dyn* 41:2711-2744. doi:10.1007/s00382-012-1607-6

799 Taylor KE, Stouffer RJ, Meehl GA (2012) An Overview of CMIP5 and the experiment design.”
800 *Bull Amer Meteorol Soc* 93:485-498. doi:10.1175/BAMS-D-11-00094.1

801 Vera C, Higgins W, Amador J, Ambrizzi T, Garreaud R, Gochis D, Gutzler D, Lettenmaier D,
802 Marengo J, Mechoso CR, Nogues-Paegle J, Silva Dias PL, Zhang C (2006) Toward a unified
803 view of the American monsoon systems. *J Clim* 19:4977-5000

804 Vizzy, EK. Cook KH, Cretat J, and Neupane N (2013) Projections of a wetter Sahel in the
805 Twenty-First Century from global and regional models. *J Clim* 26:4664-4687.
806 doi:10.1175/JCLI-D-12-00533.1

- Wang B, Ding Q (2008) Global monsoon: dominant mode of annual variation in the tropics. *Dyn Atmos Oceans* 44:165-183. doi:10.1016/j.dynatmoce.2007.05.002
- Wang B LinHo (2002) Rainy Season of the Asian–Pacific Summer Monsoon. *J Clim* 15:386-398
- Webster, PJ, Magana VO, Palmer TN, Shukla J, Tomas RA, Yanai M, Yasunari (1998) Monsoons: Processes, predictability, and the prospects for prediction. *J Geophys Res* C7 103:14451-14510
- Xie PP, Arkin PA (1997a) Global pentad precipitation analysis based on gauge observations, satellite estimates and model outputs. Extended Abstracts, Amer. Geophys. Union 1997 Fall Meeting, San Francisco, CA, Amer. Geophys. Union
- Xie PP, Arkin PA (1997b) Global precipitation: A 17-year monthly analysis based on gauge observations, satellite estimates, and numerical model outputs. *Bull Amer Meteorol Soc* 78:2539–255
- Xie PP, Janowiak JE, Arkin PA, Adler R, Gruber A, Ferraro R, Huffman GJ, Curtis S (2003) GPCP pentad precipitation analyses: an experimental dataset based on gauge observations and satellite estimates. *J Clim* 16:2197-2214
- Yin L, Fu R, Shevliakova, Dickinson RE (2012) How well can CMIP5 simulate precipitation and its controlling processes over tropical South America. *Clim Dyn* doi:10.1007/s00382-012-1582-y

Table Captions

Table 1: Modeling group, model designation, and horizontal and vertical resolutions of the atmosphere and ocean models, respectively

Table 2: Linear regression slope for the rapid fractional accumulation of rainfall between 0.2-0.8 (0.2-0.6 for Gulf of Guinea). For GPCP the time is the first pentad at which the fractional accumulation is ≥ 0.2 (denoted p0.2 in the text). For CMAP and the models the time is relative to GPCP to more clearly show the temporal biases. Bold entries are for models presented in the figures

Modelling Group	Model Designation	AGCM horizontal/vertical resolution	OGCM horizontal/vertical resolution
Canadian Centre for Climate Modelling and Analysis	CanESM2	T63 L35	256 x 192 L40
National Center for Atmospheric Research	CCSM4	1.25° lon x 0.9° lat L26	1.1° lon x 0.27°-0.54° lat L60
Centre National de Recherches Meteorologiques/Centre Europeen de Recherche et Formation Avancees en Calcul Scientifique	CNRM-CM5	TL127 L31	1° lon x 1° lat L42
Commonwealth Scientific and Industrial Research Organization in collaboration with Queensland Climate Change Centre of Excellence	CSIRO-Mk3.6.0	T63 L18	1.875° lon x ~0.9375° lat L31
LASG, Institute of Atmospheric Physics, Chinese Academy of Sciences	FGOALS-s2	R42 L26	0.5°-1° lon x 0.5°-1° lat L
NOAA Geophysical Fluid Dynamics Laboratory	GFDL-CM3 GFDL-ESM2G GFDL-ESM2M	C48 L48 M45 L24 M45 L24	360 x 200 L50 360 x 210 L63 360 x 200 L50
Met Office Hadley Centre	HadCM3 HadGEM2-CC HadGEM2-ES	N48 L19 N96 L60 N96 L38	1.25° lon x 1.25° lat L20 1° lon x 0.3°-1.0° lat L40 1° lon x 0.3°-1.0° lat L40
Institute for Numerical Mathematics	INM-CM4	5° lon x 4° lat L21	2.5° lon x 2° lat L33
Institut Pierre-Simon Laplace	IPSL-CM5A-LR IPSL-CM5A-MR	96 x 95 L39 144 x 143 L39	2° lon x 2° lat L31 2° lon x 2° lat L31

Japan Agency for Marine-Earth Science and Technology, Atmosphere and Ocean Research Institute (The University of Tokyo), and National Institute for Environmental Studies	MIROC-ESM MIROC-ESM-CHEM	T42 L80 T42 L80	256 x 192 L44 256 x 192 L44
Atmosphere and Ocean Research Institute (The University of Tokyo), National Institute for Environmental Studies, and Japan Agency for Marine-Earth Science and Technology	MIROC4h MIROC5	T213 L56 T85 L40	1280 x 912 L48 256 x 224 L50
Max Planck Institute for Meteorology	MPI-ESM-LR	T63 L47	GR15 L40
Meteorological Research Institute	MRI-CGCM3	TL159 L48	1° lon x 0.5° lat L51
Norwegian Climate Centre	NorESM1-M	144 x 96 L26	384 x 320 L53

839

840

841 **Table 2**

Model	Linear regression slope for the rapid fractional accumulation of rainfall between 0.2-0.8 (0.2-0.6 for Gulf of Guinea). For GPCP the time is the first pentad at which the fractional accumulation is ≥ 0.2 (denoted p0.2 in the text). For CMAP and the models the time is relative to GPCP to more clearly show the temporal biases. Bold entries are for models presented in the figures											
	AIR		Aus		Sahel		G. Guinea		NAM		SAM	
	Slope	Time	Slope	Time	Slope	Time	Slope	Time	Slope	Time	Slope	Time
GPCP	0.035	35	0.042	35	0.052	37	0.024	18	0.031	33	0.024	29
CMAP	0.035	0	0.043	1	0.051	0	0.021	1	0.030	0	0.025	0
CanESM2	0.035	3	0.043	0	0.034	-6	0.023	3	0.020	-10	0.031	5
CCSM4	0.035	2	0.036	-1	0.032	-6	0.024	7	0.016	-13	0.026	2
CNRM-CM5	0.034	2	0.037	-1	0.035	-3	0.020	1	0.020	-9	0.026	1
CSIRO-Mk3.6.0	0.026	2	0.046	3	0.034	-4	0.032	1	0.018	-13	0.027	2
FGOALS-s2	0.031	1	0.035	-1	0.028	-5	0.022	2	0.011	-17	0.030	4
GFDL-CM3	0.038	3	0.038	1	0.034	-4	0.029	13	0.019	-8	0.028	6
GFDL-ESM2G	0.035	3	0.040	1	0.035	-4	0.024	10	0.025	0	0.032	8
GFDL-ESM2M	0.034	2	0.045	3	0.035	-3	0.024	12	0.022	-2	0.030	7
HadCM3	0.055	4	0.038	-1	0.033	-8	0.019	5	0.020	-7	0.028	1
HadGEM2-CC	0.043	3	0.048	4	0.053	-1	0.026	6	0.022	-6	0.023	-1
HadGEM2-ES	0.048	4	0.048	4	0.048	-2	0.026	7	0.024	-4	0.024	0
INMCM4	0.030	3	0.031	-3	0.028	-9	0.018	3	0.011	-20	0.024	1
IPSL-CM5A-LR	0.043	7	0.049	4	0.049	-1	0.023	9	0.015	-13	0.036	9
IPSL-CM5A-MR	0.044	6	0.047	3	0.066	2	0.025	9	0.017	-9	0.036	9
MIROC-ESM	0.036	0	0.027	-6	0.024	-8	0.019	3	0.017	-8	0.030	2
MIROC-ESM-CHEM	0.036	0	0.028	-7	0.023	-9	0.019	3	0.016	-9	0.030	2
MIROC4h	0.041	1	0.040	0	0.036	-4	0.025	2	0.024	-4	0.027	2
MIROC5	0.033	-2	0.032	-5	0.033	-5	0.022	1	0.024	-3	0.027	1
MPI-ESM-LR	0.034	1	0.041	0	0.048	2	0.023	8	0.021	-9	0.029	3
MRI-CGCM3	0.033	6	0.046	5	0.037	-6	0.023	9	0.014	-18	0.024	2
NorESM1-M	0.040	3	0.035	-1	0.032	-7	0.018	7	0.015	-13	0.028	1

842

843

844

Figure Captions

Fig. 1 **a** Simulated and observed annual cycle of All-India rainfall (AIR), **b** standardized annual cycle of AIR. **c** accumulated AIR, and **d** fractional accumulated AIR. **e** and **f** as **c** and **d** but for observations and select models

Fig. 2 **a** GPCP accumulated rainfall for India (AIR), northern Australia (AUS), the Gulf of Guinea (GoG), the Sahel, the North American monsoon (NAM), and the South American monsoon (SAM), **b** GPCP fractional rainfall accumulations for the afore-mentioned regions. **c** GPCP and CMAP linear regression slopes of the rapid fractional rainfall accumulations over the range 0.2-0.8 (0.2-0.6 for Sahel) vs. the first pentad at which the fractional accumulation ≥ 0.2 . Note: for Southern Hemisphere locations (AUS and SAM) the pentads were reordered to July-June prior to the analysis

Fig. 3 Simulated and observed rainfall accumulations for **a** northern Australia (AUS), **b** the Sahel, **c** the Gulf of Guinea (GoG), **d** the North American monsoon (NAM), and **e** the South American monsoon (SAM). Simulated and observed fractional rainfall accumulations for **f** northern Australia (AUS), **g** the Sahel, **h** the Gulf of Guinea (GoG), **i** the North American monsoon (NAM), and **j** the South American monsoon (SAM). Note: for Southern Hemisphere locations (AUS and SAM) the pentads were reordered to July-June prior to the analysis

Fig. 4 **a** Simulated and observed linear regression slopes of the rapid fractional rainfall accumulations over the range 0.2-0.8 (0.2-0.6 for Gulf of Guinea) vs. the first pentad at which the fractional accumulation ≥ 0.2 . **a** All-India rainfall (AIR), **b** northern Australia (AUS), **c** the Sahel, **d** Gulf of Guinea (GoG), **e** the North American monsoon (NAM), and **f** the South American monsoon (SAM). In each panel the observations are contained within the black ellipse. Note: NAM has a broader x-axis scale

Fig. 5 Fractional accumulations at pentad 31 (June 2) **a** GPCP, **b** CSIRO-MK3.6.0, **c** HadCM3, and **d** MIROC-ESM. Fractional accumulations during boreal summer (pentad 55 - pentad 31) **e** GPCP, **f** CSIRO-MK3.6.0, **g** HadCM3, and **h** MIROC-ESM

Fig. 6 The pentad at which a fractional accumulation of 0.2 is reached **a** GPCP, **b** CSIRO-MK3.6.0, **c** HadCM3, and **d** MIROC-ESM. Interannual variability of the pentad at which a fractional accumulation of 0.2 is reached from an analysis of each year of data **e** GPCP, **f** CSIRO-MK3.6.0, **g** HadCM3, and **h** MIROC-ESM

Fig. 7 Fractional accumulations during Austral summer (pentad 55 - pentad 31) **a** GPCP, **b** CanESM2, **c** MIROC-ESM, and **d** MRC-CGCM3. Interannual variability of the pentad at which a fractional accumulation of 0.2 is reached from an analysis of each year of data **e** GPCP, **f** CanESM2, **g** MIROC-ESM, and **h** MRI-CGCM3. Note: the pentads were reordered to July-June prior to the analysis

Fig. 8 **a** Annual cycle of Sahel rainfall, **b** standardized annual cycle of Sahel rainfall. Fractional accumulations at pentad 31 (June 2) **c** GPCP and **d** MIROC-ESM-CHEM. Fractional accumulations during boreal summer (pentad 55 - pentad 31) **e** GPCP and **f** MIROC-ESM-CHEM

Fig. 9 Interannual variability of the pentad at which a fractional accumulation ≥ 0.2 is reached from an analysis of each year of data **a** GPCP, **b** IPSL-CM5A-LR, **c** MIROC-ESM-CHEM

Fig. 10 **a** GPCP fractional accumulations at pentad 31 (June 2). The pentad at which **b** CMAP, **c** GFDL-ESM2G, and **d** INMCM4 reach the GPCP pentad 31 fractional accumulations in **a**. **e** GPCP fractional accumulations at pentad 31 (November 29). The pentad at which **f** CMAP, **g** HadGEM2-ES, and **h** IPSL-CM5A-MR reach the GPCP pentad 31 fractional accumulations in (e). Note: for **e-h** the pentads were reordered to July-June prior to the analysis

Fig. 11 Fractional accumulations during boreal summer (pentad 55 - pentad 31) **a** GPCP, **b** GFDL-ESM2G, and **c** INMCM4. Fractional accumulations during Austral summer (pentad 55 - pentad 31) **d** GPCP, **e** HadGEM2-ES, and **f** IPSL-CM5A-MR. Note: for **d-f** the pentads were reordered to July-June prior to the analysis

Fig. 12 Interannual variability of the pentad at which a fractional accumulation ≥ 0.2 is reached from an analysis of each year of data **a** GPCP, **b** GFDL-ESM2G, **c** INMCM4, **d** GPCP, **e** HadGEM2-ES, and **f** IPSL-CM5A-MR. Note: for **d-f** the pentads were reordered to July-June prior to the analysis

Fig. 13 Method 1 duration calculated as $1 + p_{0.8} - p_{0.2}$ **a** GPCP, **b** CSIRO-MK3.6.0, **c** HadCM3, and **d** MIROC-ESM. Method 2 duration calculated as $1 + \text{pentad the model reaches the GPCP fractional accumulation at } p_{55} - \text{pentad the model reaches the GPCP fractional accumulation at } p_{31}$ **e** CMAP, **f** CSIRO-MK3.6.0, **g** HadCM3, and **h** MIROC-ESM

Fig. 14 Method 2 duration calculated as $1 + \text{pentad the model reaches the GPCP fractional accumulation at } p_{55} - \text{pentad the model reaches the GPCP fractional accumulation at } p_{31}$ **a** CanESM2, **b** MRI-CGCM3, **c** CMAP, **d** MIROC-ESM-CHEM, **e** CMAP, **f** INMCM4, **g** HadGEM2-ES, and **h** IPSL-CM5A-MR. Note: for Australia and South America the pentads were reordered to July-June prior to the analysis

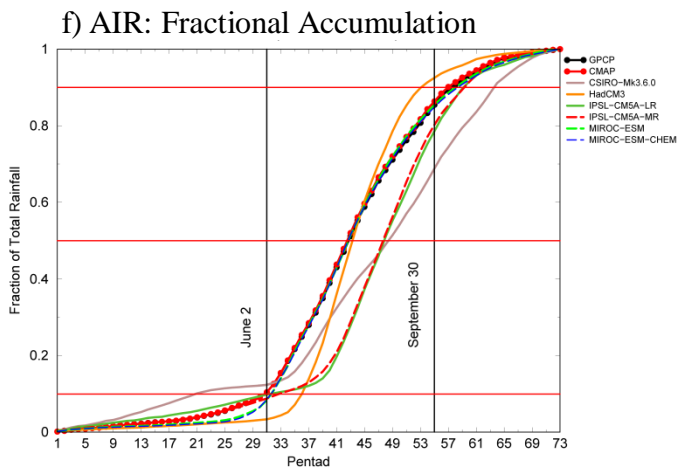
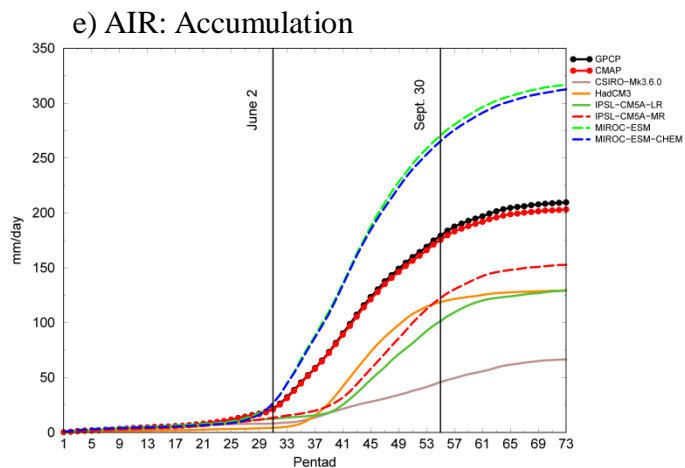
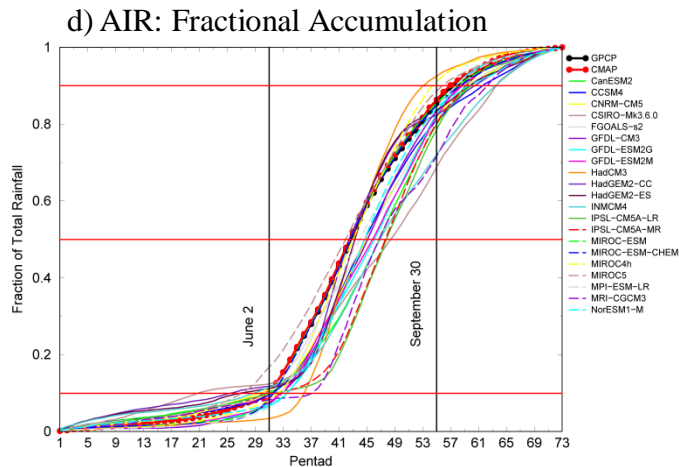
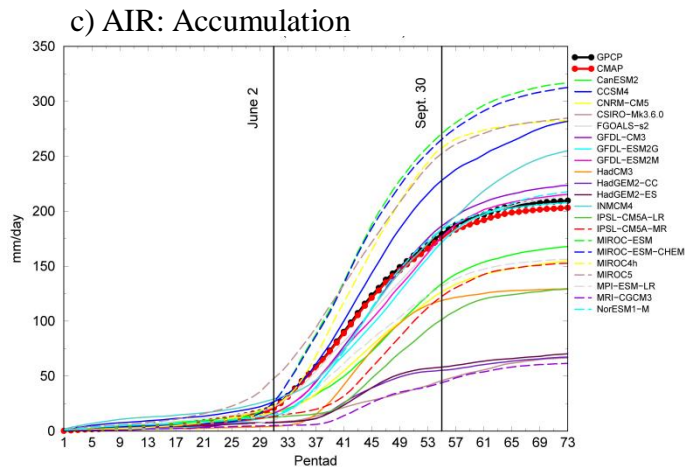
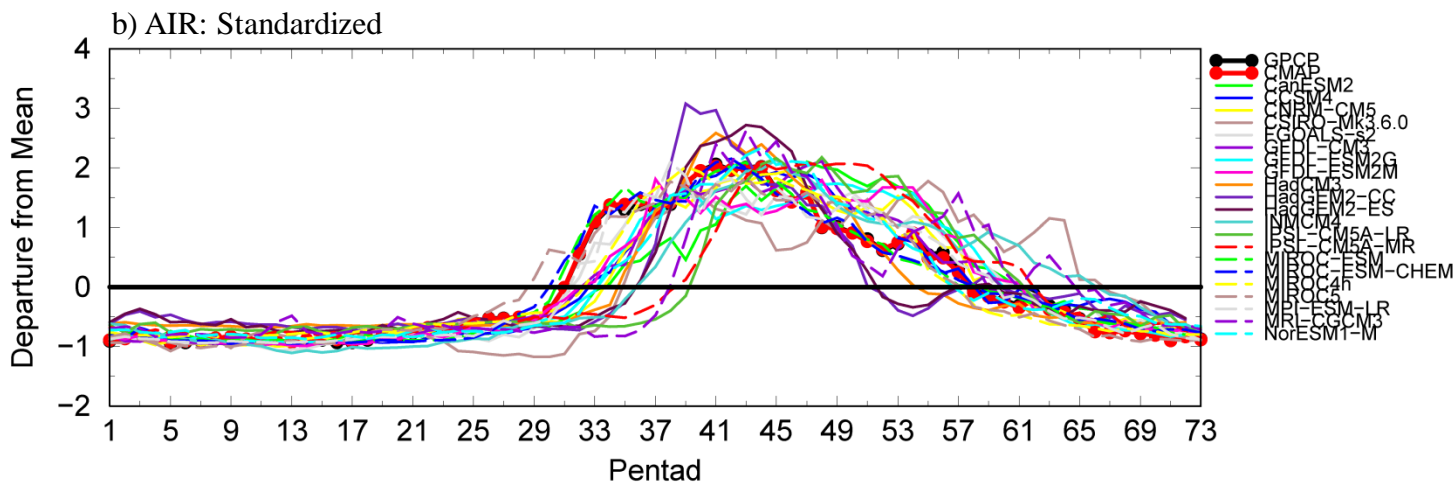
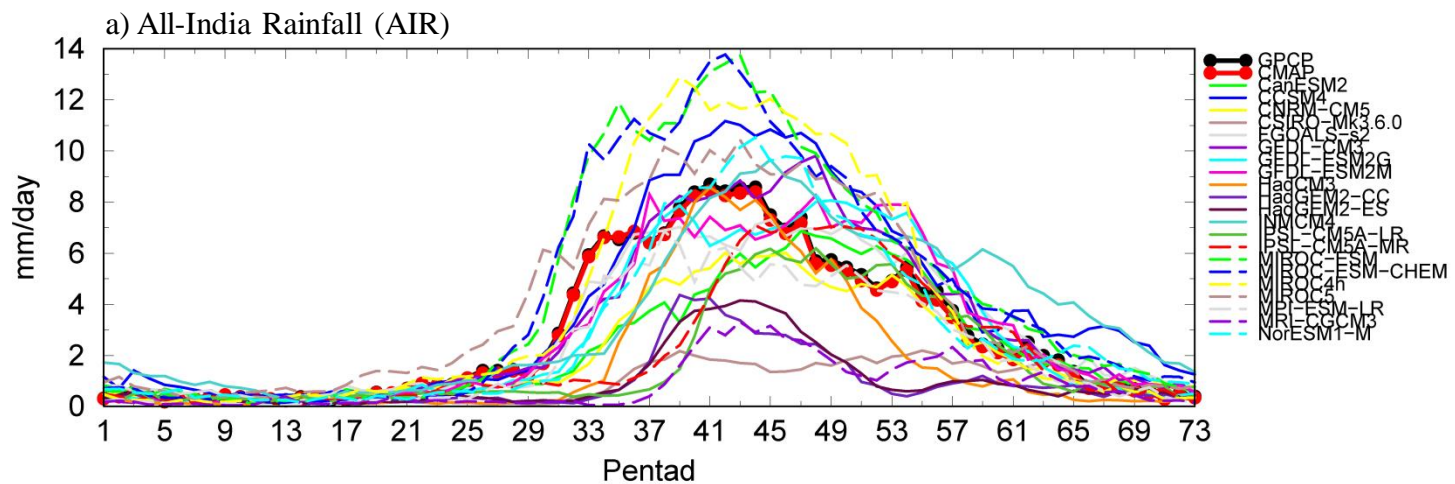


Fig. 1 **a** Simulated and observed annual cycle of All-India rainfall (AIR), **b** standardized annual cycle of AIR. **c** accumulated AIR, and **d** fractional accumulated AIR. **e** and **f** as **c** and **d** but for observations and select models

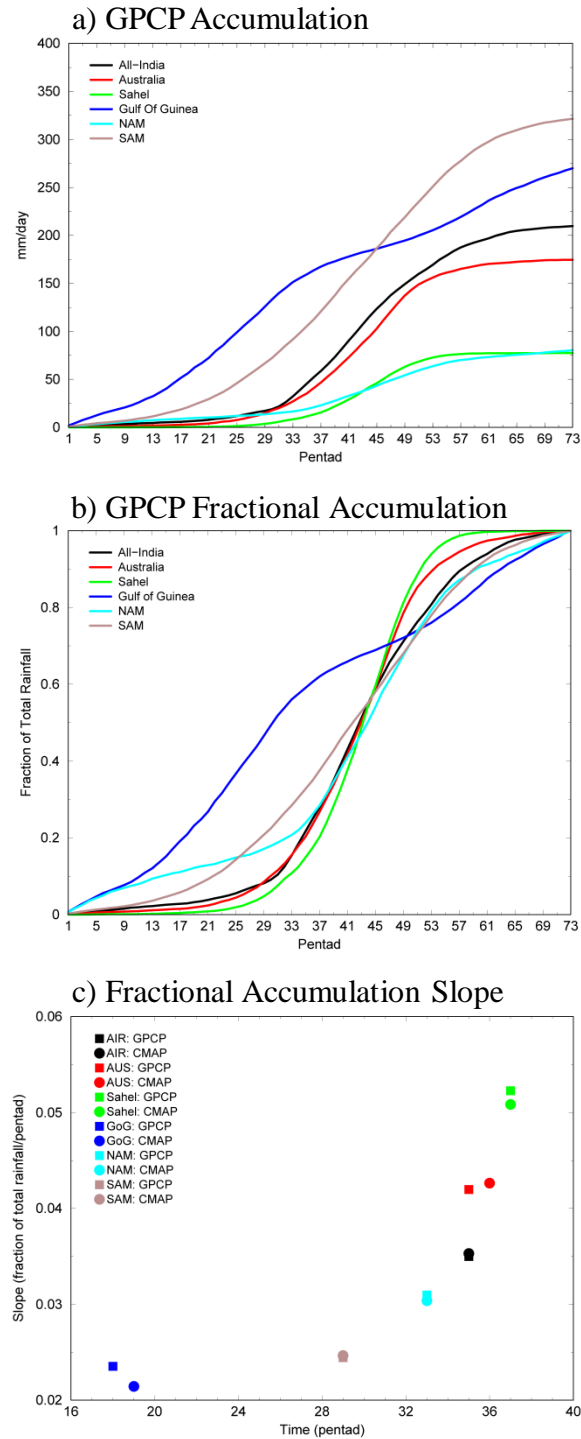
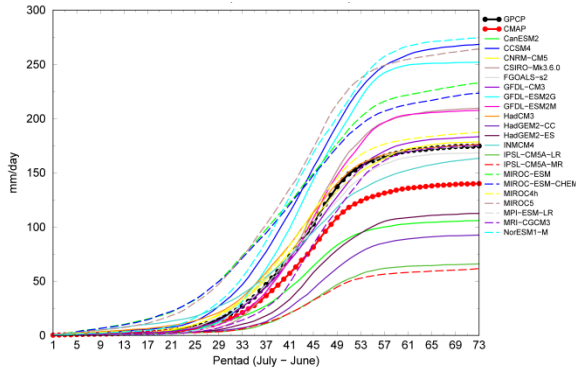
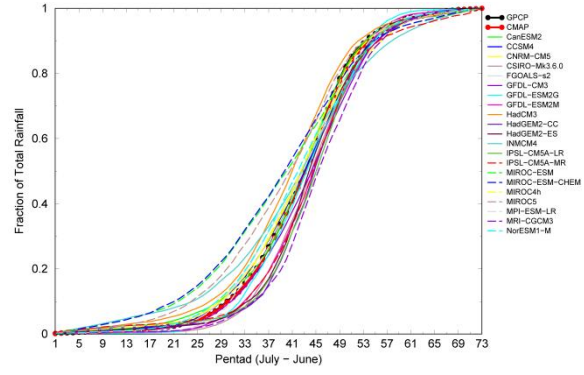


Fig. 2 a GPCP accumulated rainfall for India (AIR), northern Australia (AUS), the Gulf of Guinea (GoG), the Sahel, the North American monsoon (NAM) and the South American monsoon (SAM), **b** GPCP fractional rainfall accumulations for the afore-mentioned regions. **c** GPCP and CMAP linear regression slopes of the fractional rainfall accumulations over the range 0.2-0.8 (0.2-0.6 for Sahel) vs. the first pentad at which the fractional accumulation ≥ 0.2 . Note: for Southern Hemisphere locations (AUS and SAM) the pentads were reordered to July-June prior to the analysis

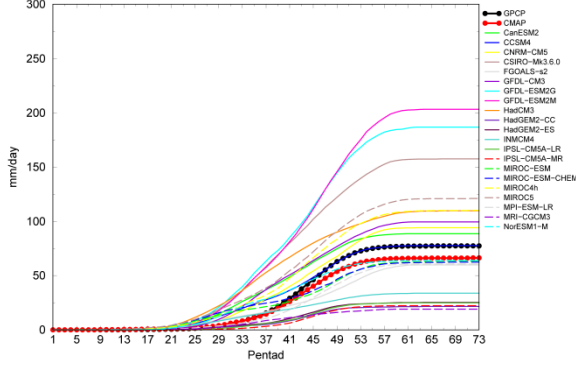
a) AUS Accumulation



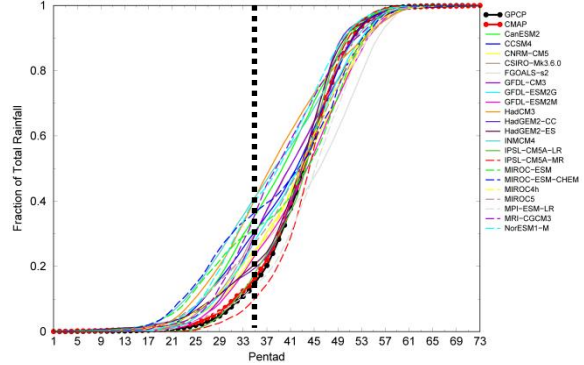
f) AUS Fractional Accumulation



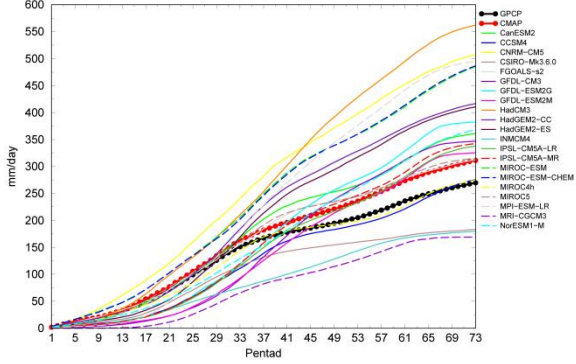
b) Sahel Accumulation



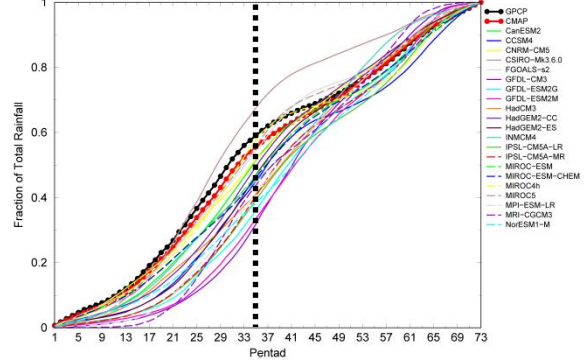
g) Sahel Fractional Accumulation



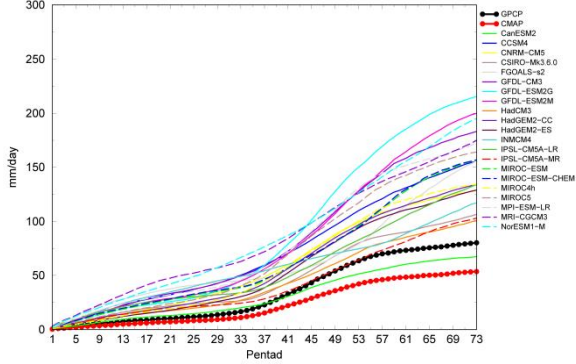
c) GoG Accumulation



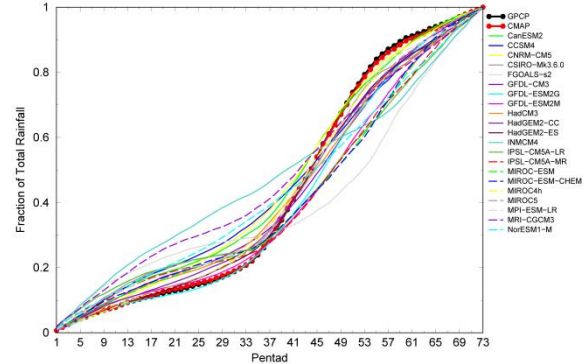
h) GoG Fractional Accumulation



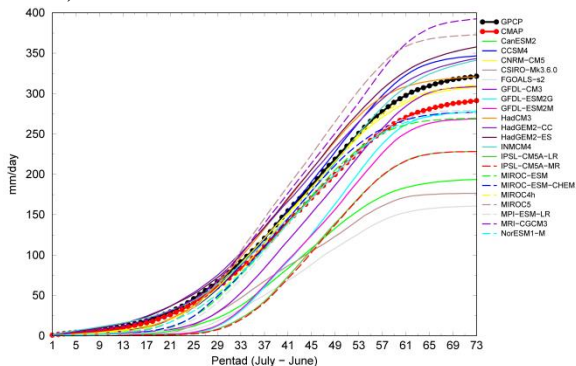
d) NAM Accumulation



i) NAM Fractional Accumulation



e) SAM Accumulation



j) SAM Fractional Accumulation

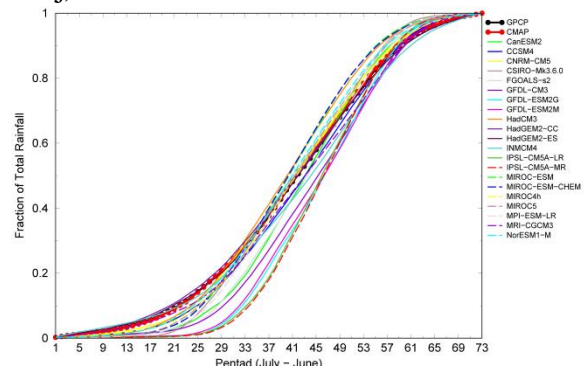


Fig. 3 Simulated and observed rainfall accumulations for **a** northern Australia (AUS), **b** the Sahel, **c** the Gulf of Guinea (GoG), **d** the North American monsoon (NAM), and **e** the South American monsoon (SAM). Simulated and observed fractional rainfall accumulations for **f** northern Australia (AUS), **g** the Sahel, **h** the Gulf of Guinea (GoG), **i** the North American monsoon (NAM), and **j** the South American monsoon (SAM). Note: for Southern Hemisphere locations (AUS and SAM) the pentads were reordered to July-June prior to the analysis

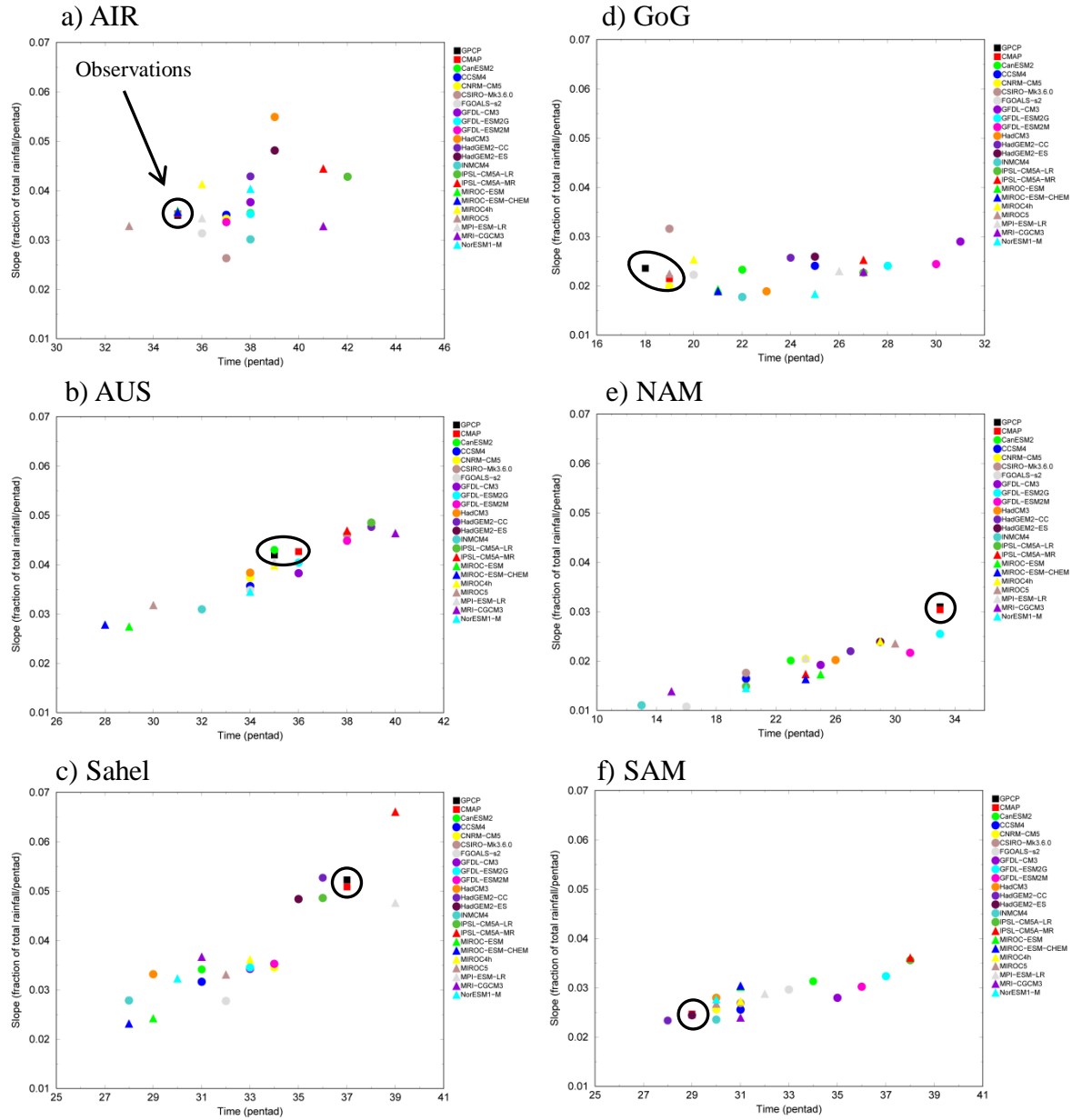


Fig. 4 a Simulated and observed linear regression slopes of the fractional rainfall accumulations over the range 0.2-0.8 (0.2-0.6 for Gulf of Guinea) vs. the first pentad at which the fractional accumulation ≥ 0.2 . **a** All-India rainfall (AIR), **b** northern Australia (AUS), **c** the Sahel, **d** Gulf of Guinea (GoG), **e** the North American monsoon (NAM), and **f** the South American monsoon (SAM). In each panel the observations are contained within the black ellipse. Note: NAM has a broader x-axis scale

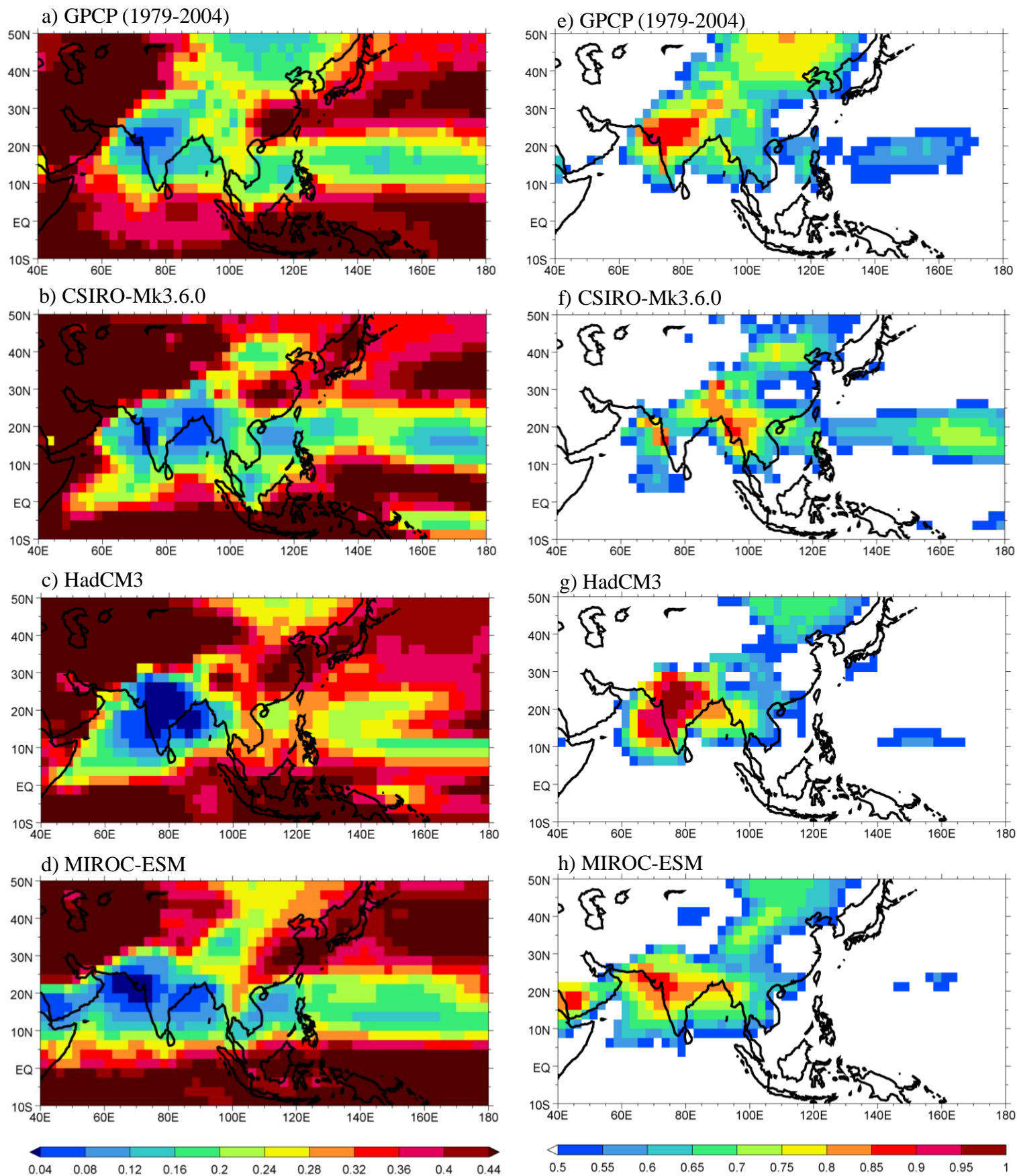


Fig. 5 Fractional accumulations at pentad 31 (June 2) **a** GPCP, **b** CSIRO-MK3.6.0, **c** HadCM3, and **d** MIROC-ESM. Fractional accumulations during boreal summer (pentad 55 - pentad 31) **e** GPCP, **f** CSIRO-MK3.6.0, **g** HadCM3, and **h** MIROC-ESM

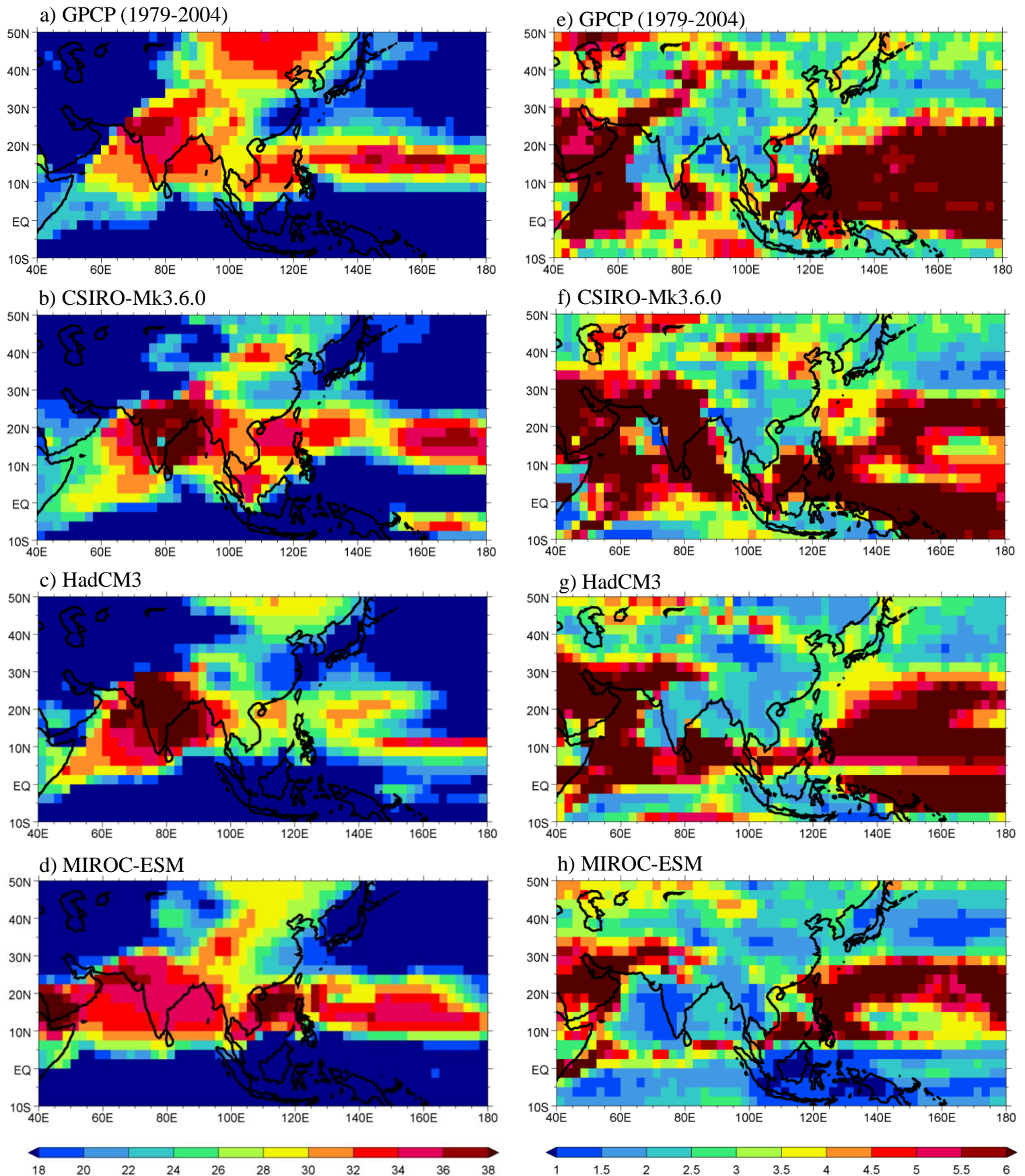


Fig. 6 The pentad at which a fractional accumulation of 0.2 is reached **a** GPCP, **b** CSIRO-MK3.6.0, **c** HadCM3, and **d** MIROC-ESM. Interannual variability of the pentad at which a fractional accumulation of 0.2 is reached from an analysis of each year of data **e** GPCP, **f** CSIRO-MK3.6.0, **g** HadCM3, and **h** MIROC-ESM

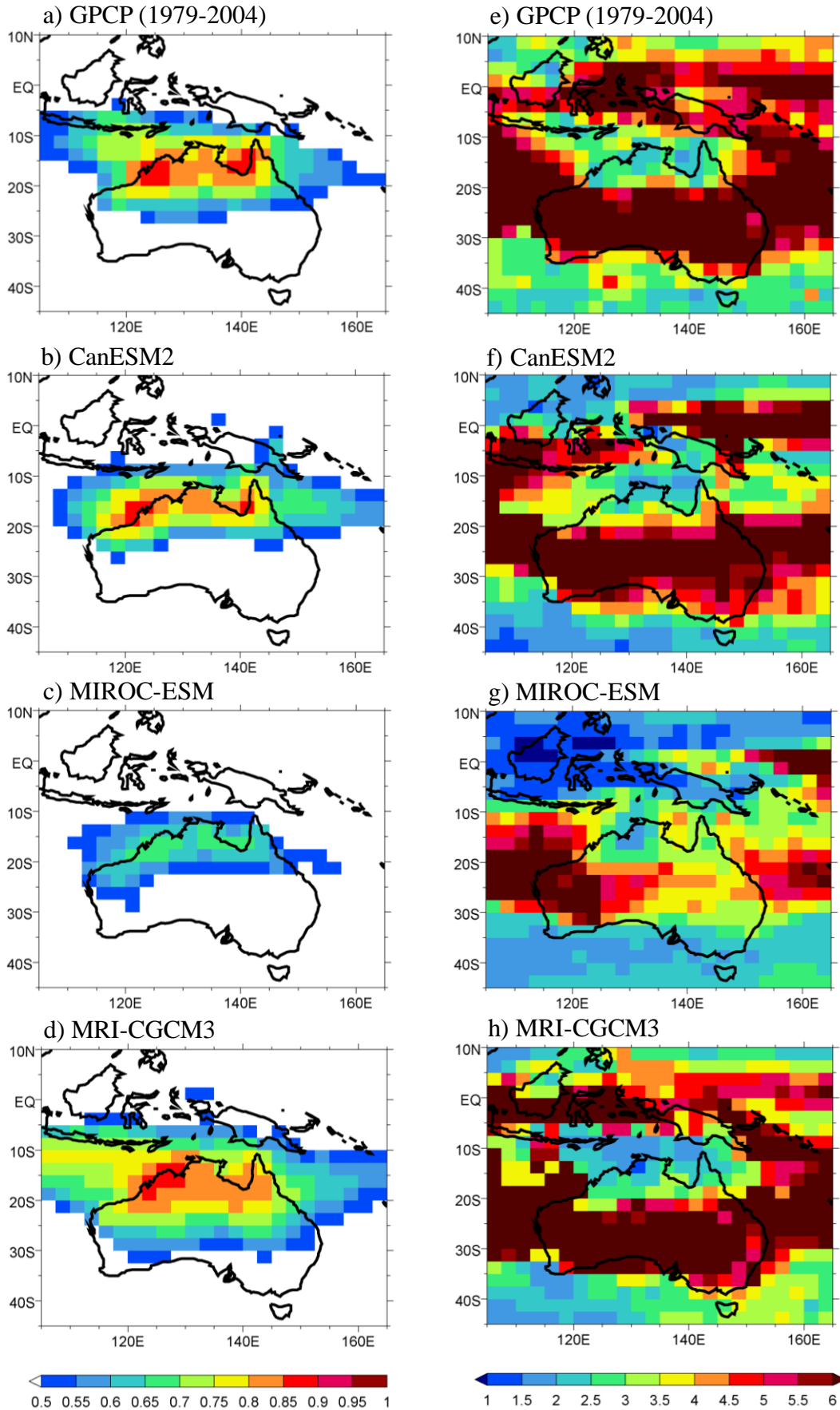


Fig. 7 Fractional accumulations during Austral summer (pentad 55 - pentad 31) **a** GPCP, **b** CanESM2, **c** MIROC-ESM, and **d** MRI-CGCM3. Interannual variability of the pentad at which a fractional accumulation of 0.2 is reached from an analysis of each year of data **e** GPCP, **f** CanESM2, **g** MIROC-ESM, and **h** MRI-CGCM3. Note: the pentads were reordered to July-June prior to the analysis

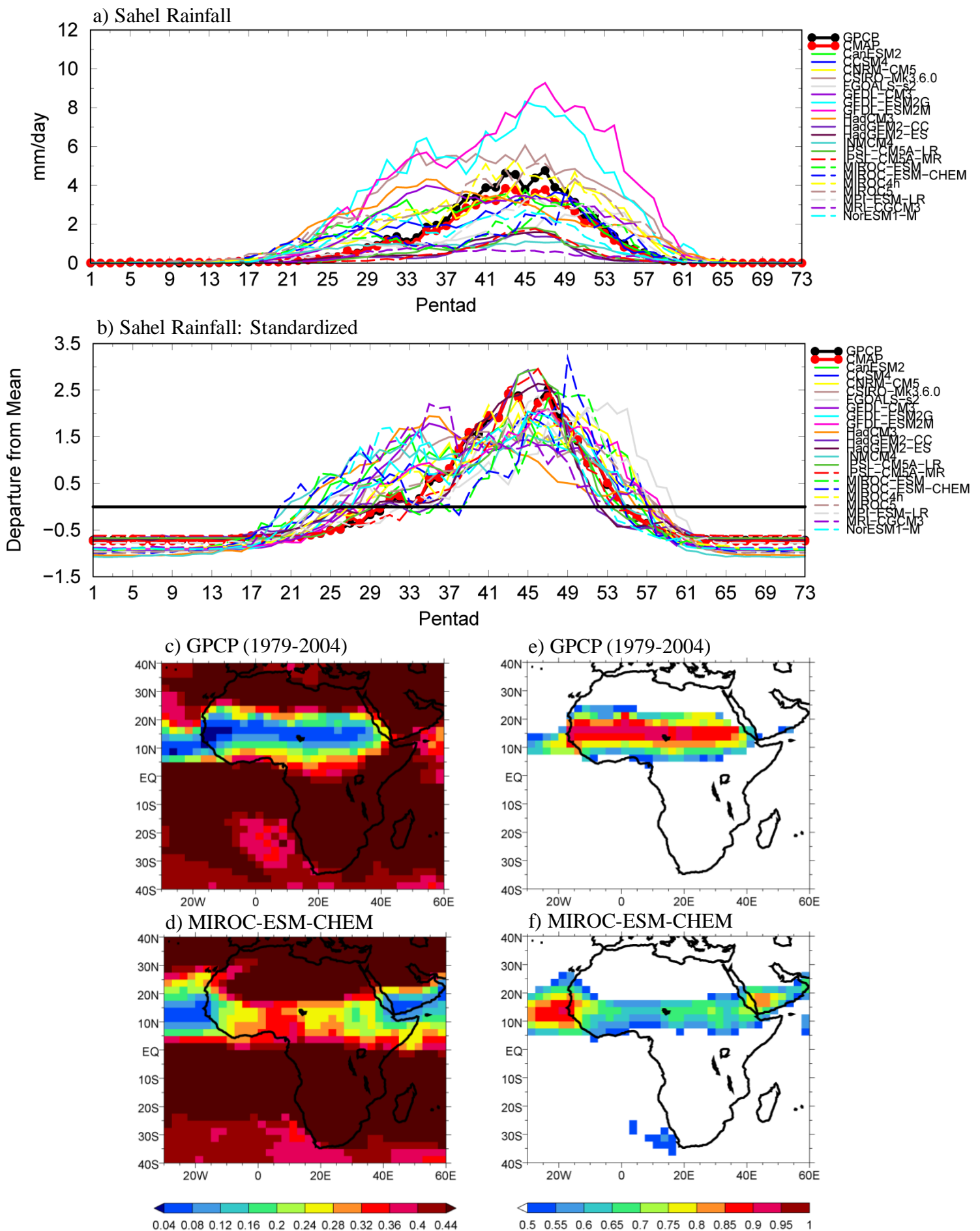


Fig. 8 **a** Annual cycle of Sahel rainfall, **b** standardized annual cycle of Sahel rainfall. Fractional accumulations at pentad 31 (June 2) **c** GPCP and **d** MIROC-ESM-CHEM. Fractional accumulations during boreal summer (pentad 55 - pentad 31) **e** GPCP and **f** MIROC-ESM-CHEM

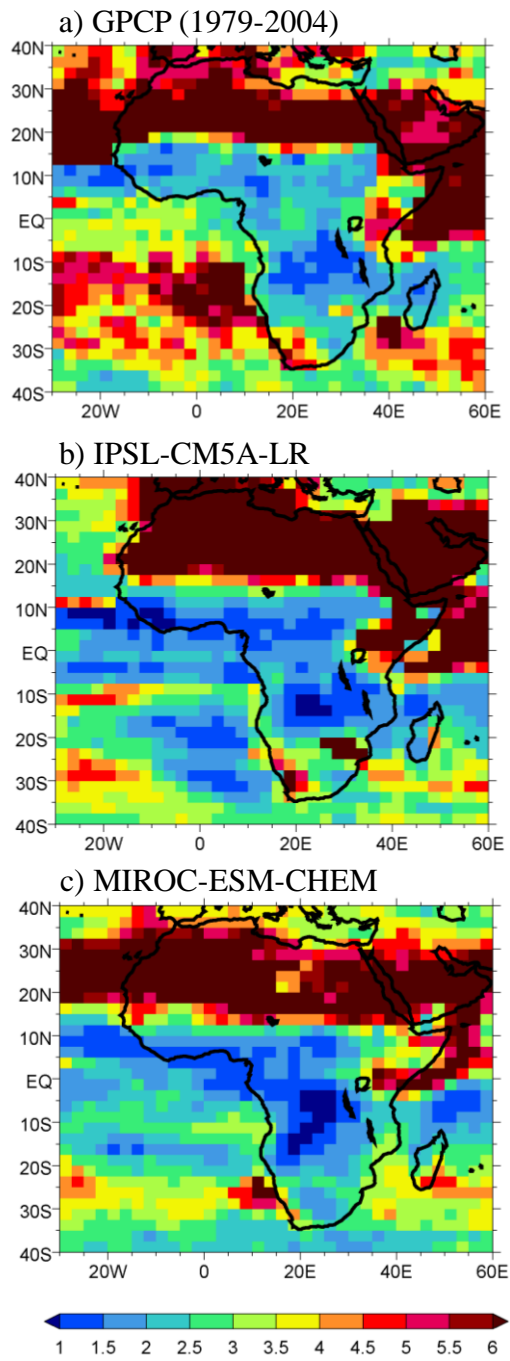


Fig. 9 Interannual variability of the pentad at which a fractional accumulation ≥ 0.2 is reached from an analysis of each year of data **a** GPCP, **b** IPSL-CM5A-LR, **c** MIROC-ESM-CHEM

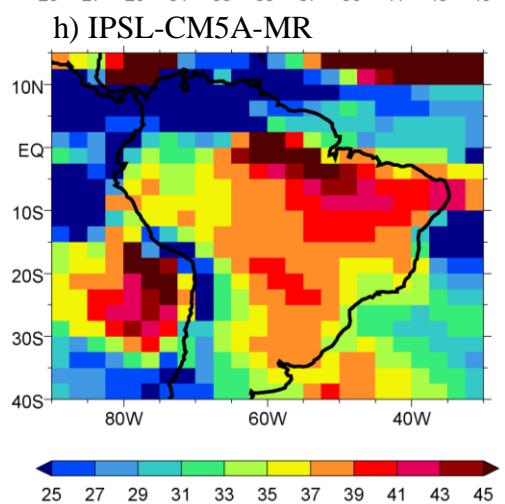
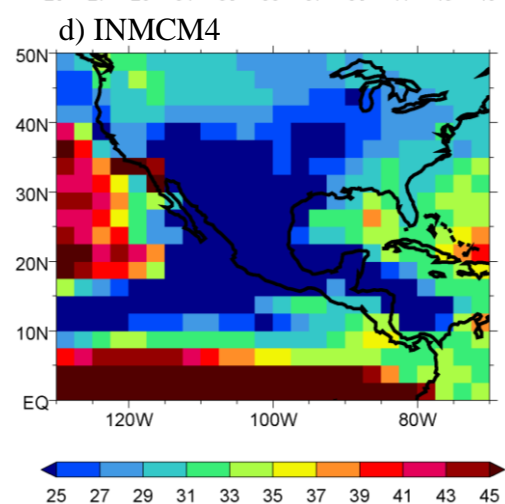
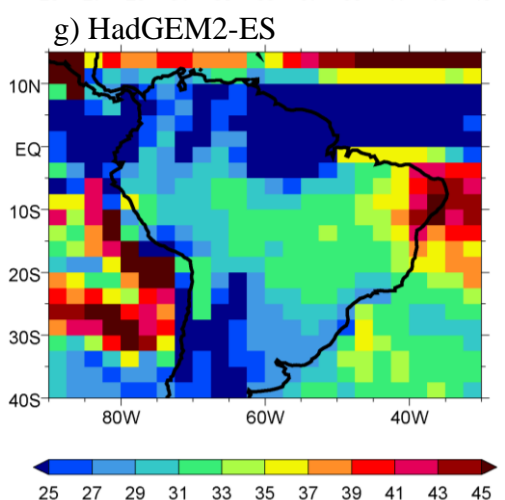
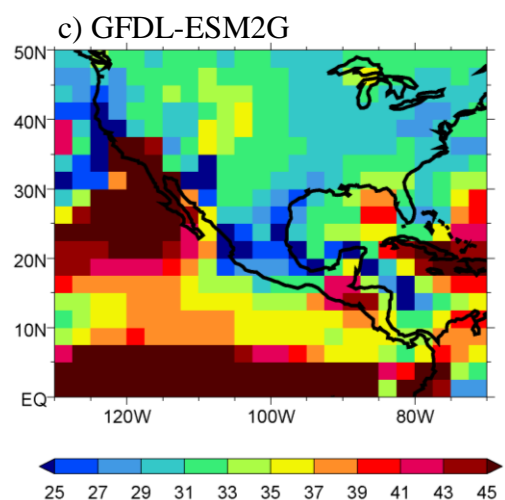
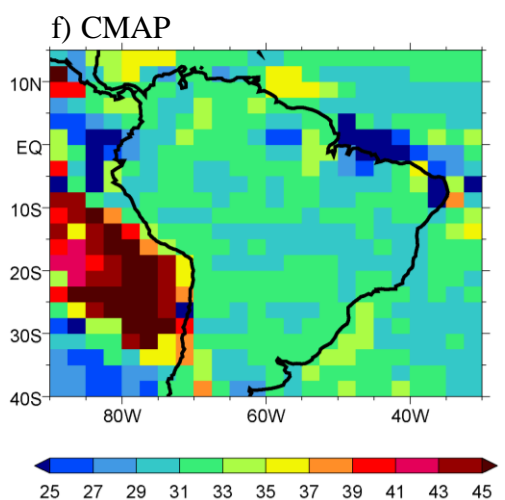
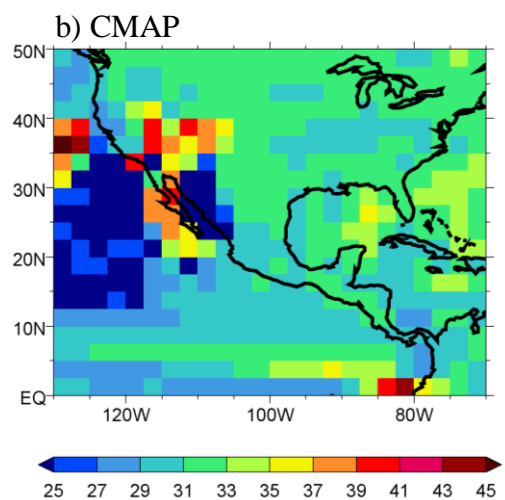
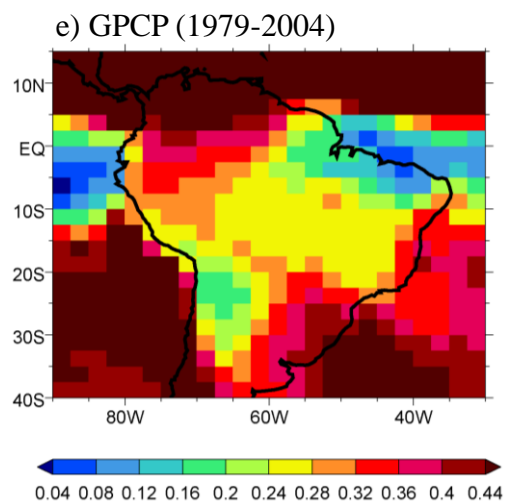
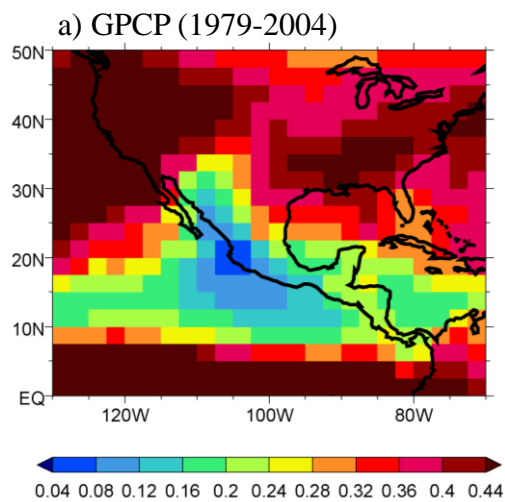


Fig. 10 **a** GPCP fractional accumulations at pentad 31 (June 2). The pentad at which **b** CMAP, **c** GFDL-ESM2G, and **d** INMCM4 reach the GPCP pentad 31 fractional accumulations in **a**. **e** GPCP fractional accumulations at pentad 31 (November 29). The pentad at which **f** CMAP, **g** HadGEM2-ES, and **h** IPSL-CM5A-MR reach the GPCP pentad 31 fractional accumulations in (e). Note: for **e-h** the pentads were reordered to July-June prior to the analysis

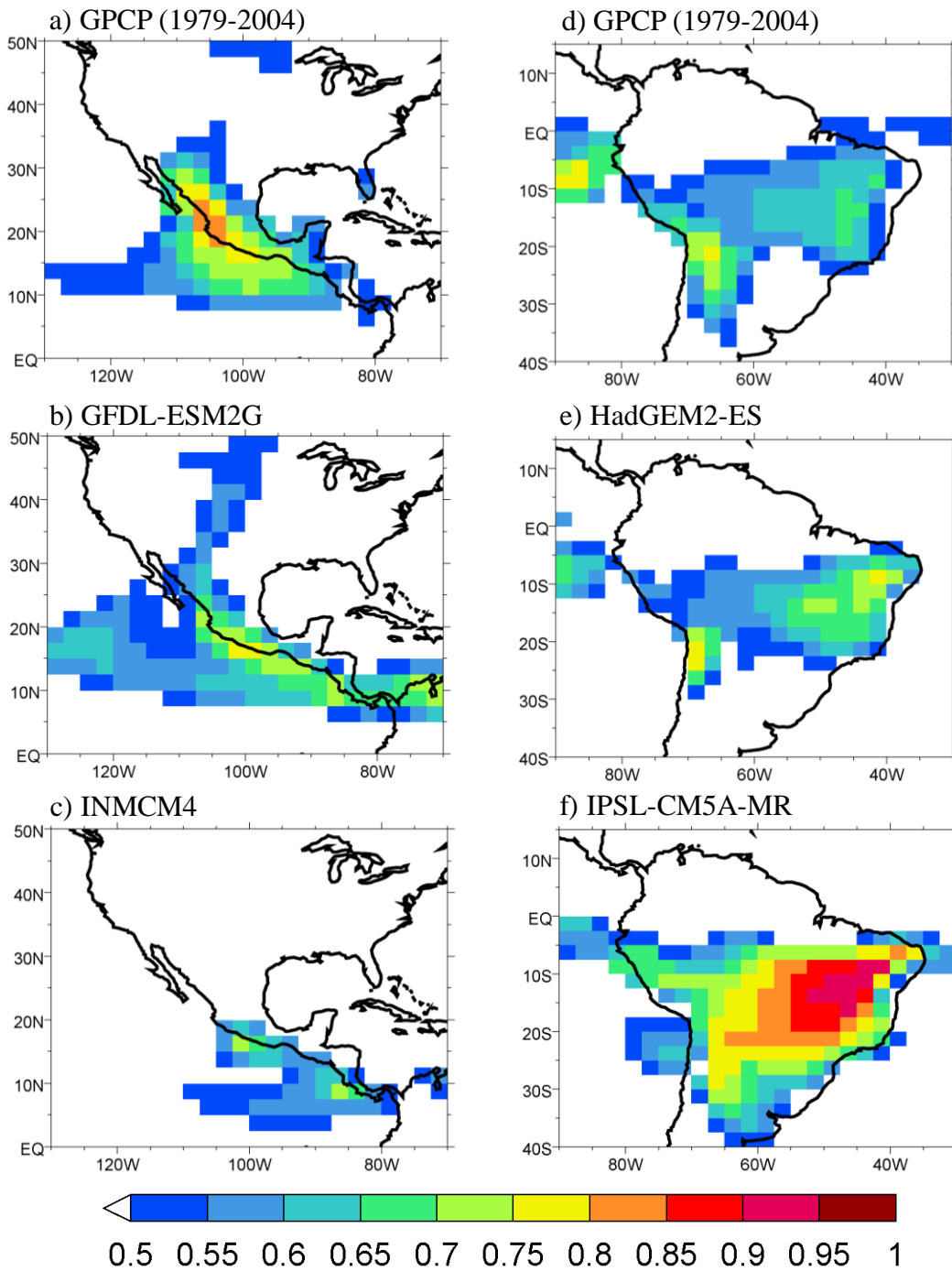


Fig. 11 Fractional accumulations during boreal summer (pentad 55 - pentad 31) **a** GPCP, **b** GFDL-ESM2G, and **c** INMCM4. Fractional accumulations during Austral summer (pentad 55 - pentad 31) **d** GPCP, **e** HadGEM2-ES, and **f** IPSL-CM5A-MR. Note: for **d-f** the pentads were reordered to July-June prior to the analysis

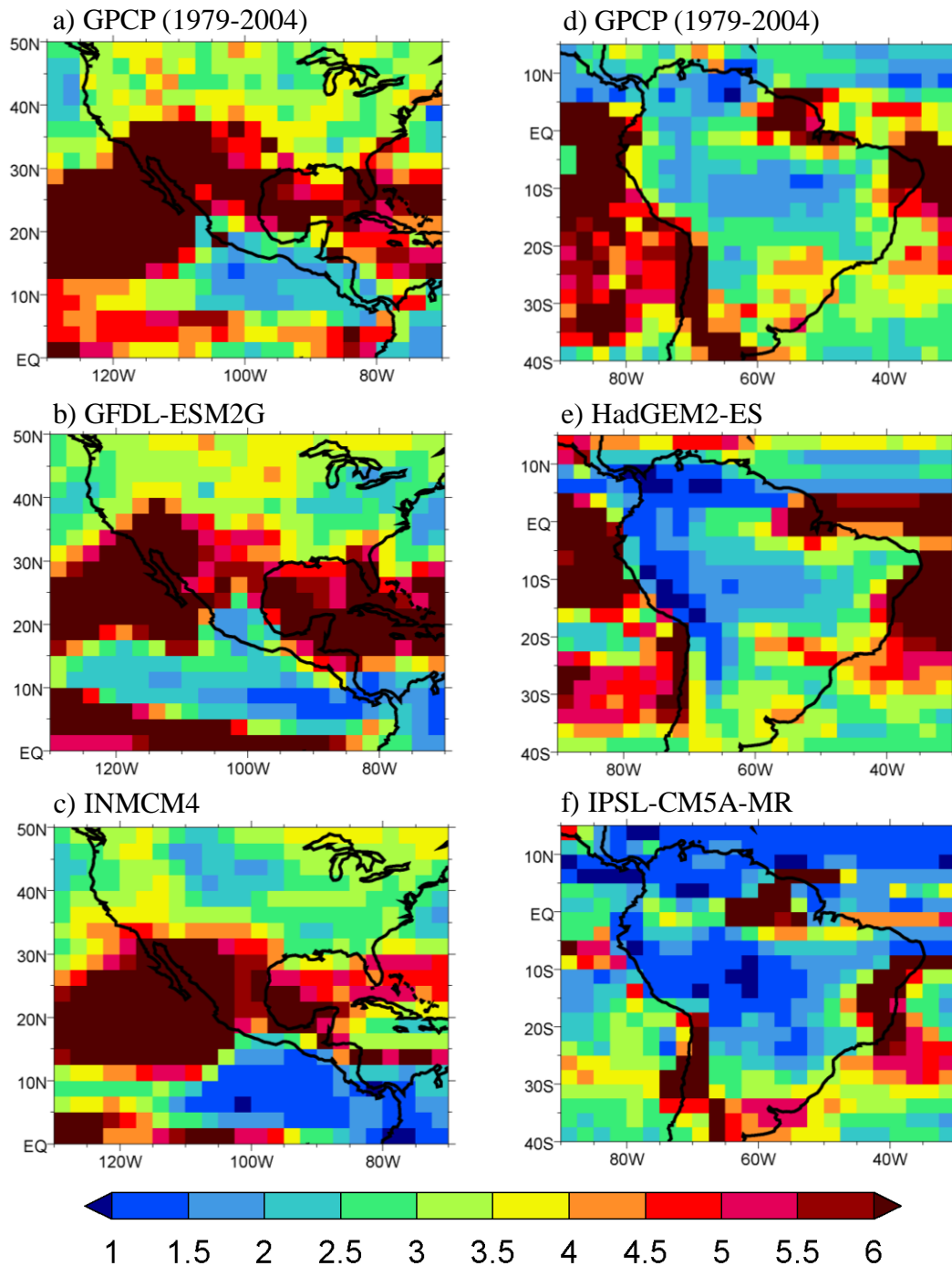


Fig. 12 Interannual variability of the pentad at which a fractional accumulation ≥ 0.2 is reached from an analysis of each year of data **a** GPCP, **b** GFDL-ESM2G, **c** INMCM4, **d** GPCP, **e** HadGEM2-ES, and **f** IPSL-CM5A-MR. Note: for **d-f** the pentads were reordered to July-June prior to the analysis

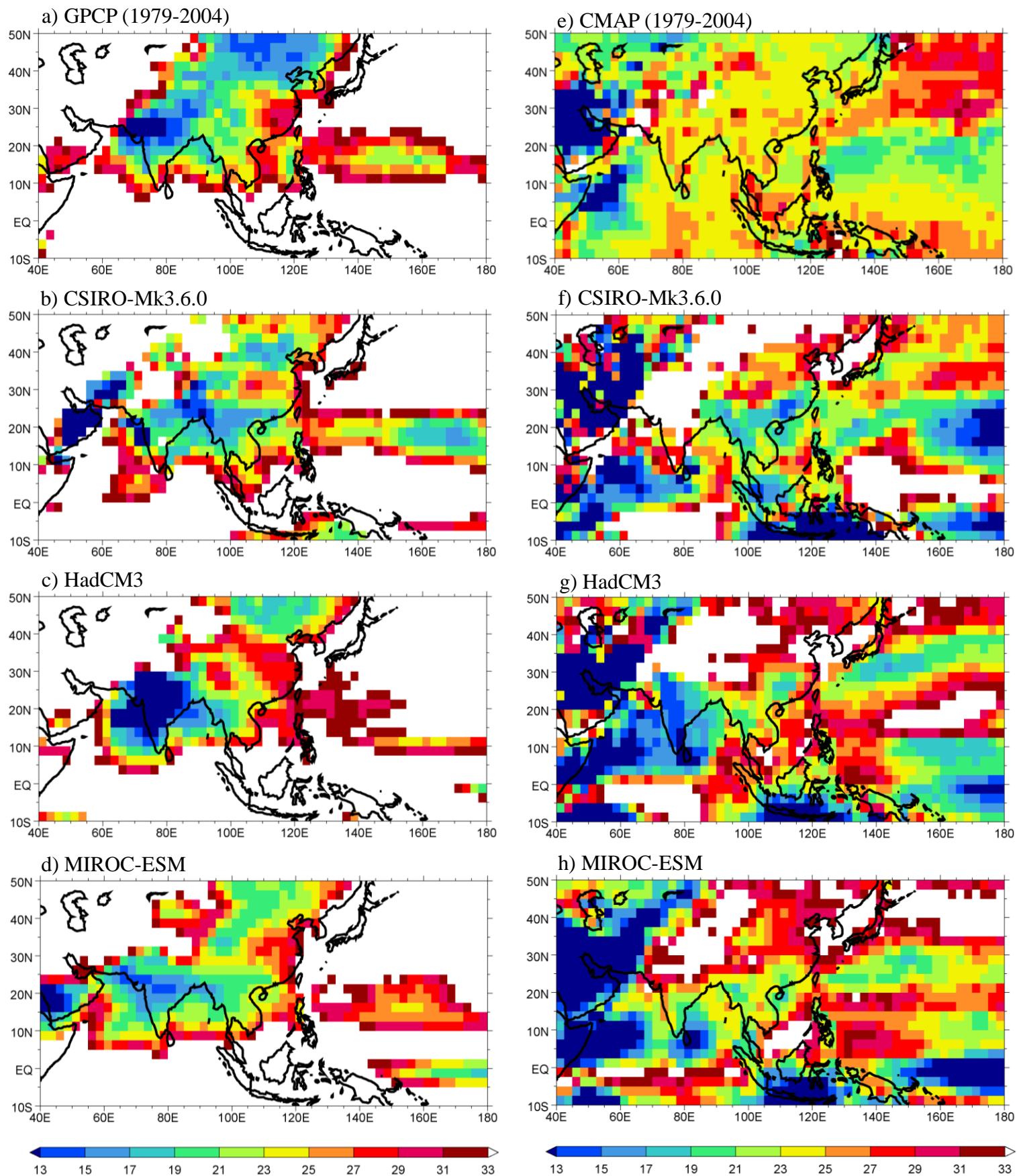


Fig. 13 Method 1 duration calculated as $1 + p_{0.8} - p_{0.2}$ **a** GPCP, **b** CSIRO-MK3.6.0, **c** HadCM3, and **d** MIROC-ESM. Method 2 duration calculated as $1 + \text{pentad the model reaches the GPCP fractional accumulation at } p_{55} - \text{pentad the model reaches the GPCP fractional accumulation at } p_{31}$ **e** CMAP, **f** CSIRO-MK3.6.0, **g** HadCM3, and **h** MIROC-ESM

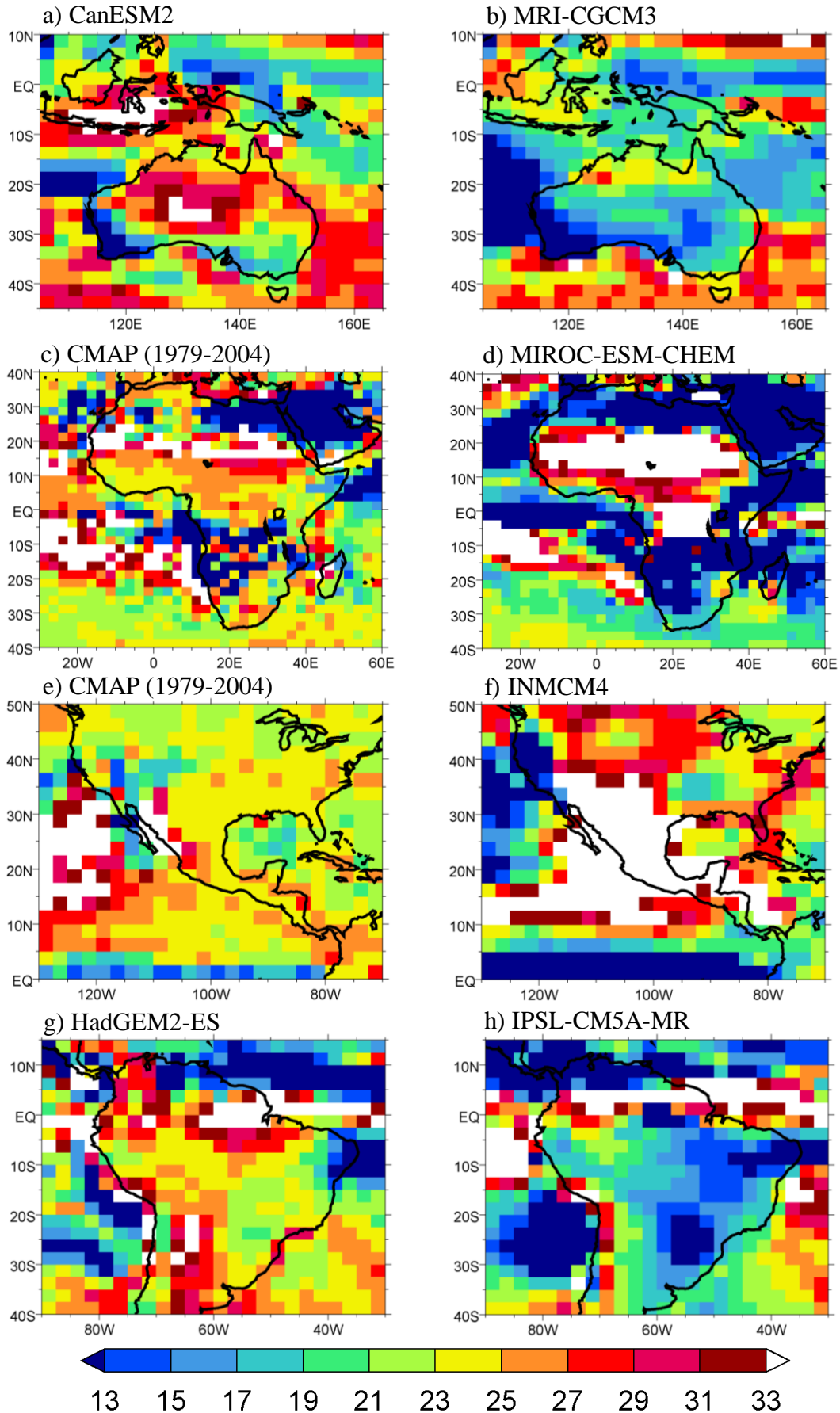


Fig. 14 Method 2 duration calculated as 1 + pentad the model reaches the GPCP fractional accumulation at p55 – pentad the model reaches the GPCP fractional accumulation at p31 **a** CanESM2, **b** MRI-CGCM3, **c** CMAP, **d** MIROC-ESM-CHEM, **e** CMAP, **f** INMCM4, **g** HadGEM2-ES, and **h** IPSL-CM5A-MR. Note: for Australia and South America the pentads were reordered to July-June prior to the analysis